



저작자표시-비영리-변경금지 2.0 대한민국

이용자는 아래의 조건을 따르는 경우에 한하여 자유롭게

- 이 저작물을 복제, 배포, 전송, 전시, 공연 및 방송할 수 있습니다.

다음과 같은 조건을 따라야 합니다:



저작자표시. 귀하는 원저작자를 표시하여야 합니다.



비영리. 귀하는 이 저작물을 영리 목적으로 이용할 수 없습니다.



변경금지. 귀하는 이 저작물을 개작, 변형 또는 가공할 수 없습니다.

- 귀하는, 이 저작물의 재이용이나 배포의 경우, 이 저작물에 적용된 이용허락조건을 명확하게 나타내어야 합니다.
- 저작권자로부터 별도의 허가를 받으면 이러한 조건들은 적용되지 않습니다.

저작권법에 따른 이용자의 권리는 위의 내용에 의하여 영향을 받지 않습니다.

이것은 [이용허락규약\(Legal Code\)](#)을 이해하기 쉽게 요약한 것입니다.

[Disclaimer](#)

석사학위논문

Surface Plasmon Damping Effect and Refractive  
Index Sensitivity of Single Gold Nanoparticles

단일 금 나노 입자의 화학적 표면 감쇠  
효과와 주변 매질 굴절률에 따른 민감도

The Graduate School of the University of Ulsan

Department of Chemistry

Hui Bin Jeon



Surface Plasmon Damping Effect and Refractive  
Index Sensitivity of Single Gold Nanoparticles

Professor: Ji Won Ha

A Dissertation Submitted to The Graduate  
School of The University of Ulsan

in Partial Fulfillment of The Requirements

for The Degree of Master of Science in

Department of Chemistry

by Hui Bin Jeon

University of Ulsan, Ulsan, Korea

February, 2020

This certifies that the dissertation of Hui Bin Jeon is approved.

---

Committee                      Ji Won Ha

---

Committee                      Young Il Lee

---

Committee                      Jong Wook Hong

Department of Chemistry

University of Ulsan, Ulsan, Korea

February, 2020

## 국문 초록

플라즈모닉 금 나노 입자는 국지 표면 플라즈몬 공명 (Localized Surface Plasmon Resonance, LSPR) 현상에 의해 그들의 모양, 크기, 주변 매질의 굴절률(RI) 등에 따라 독특한 광학적 특성을 가진다. 이러한 금 나노 입자는 생체 친화적이고, 높은 화학적 안정성을 가지며 표면 개질이 쉽다는 장점이 있어 많은 분야에서 응용되고 있다. 특히 금 나노 입자는 주변 매질의 굴절률에 따른 스펙트럼의 이동으로 LSPR 바이오 센서에 사용될 수 있을 뿐만 아니라 표면에 부착되는 물질에 의한 화학적 계면 감쇠 (Chemical Interface Damping, CID) 현상으로 인해 야기되는 LSPR 선폭의 변화를 바탕으로 바이오센서, 약물 전달 및 에너지 분야 등 응용 분야가 다양하다. 하지만 아직까지 화학적 계면 감쇠 현상에 대한 정보가 많이 부족하며 금 나노 입자의 응용 가능성을 높이기 위해 단일 입자 수준에서의 더 많은 연구가 필요하다.

본 연구에서는 주사 전자 현미경 (Scanning Electron Microscope, SEM)과 암시야 (Dark-Field, DF) 현미경, 자외선-가시광선 분광기 (UV-Vis spectroscope, UV-Vis)를 사용하여 단일 금 나노 입자의 광특성을 분석하였다. 첫째, 상대적으로 잘 알려지지 않은 금 나노큐브

(gold nanocube, AuNC)의 광특성에 대해 알아보았다. 둘째, 크기는 같고 모양이 다른 구형의 금 나노 입자 (gold nanosphere, AuNS)와 AuNC를 사용하여 주변 매질 굴절률에 따른 민감도 (RI sensitivity)에 금 나노 입자의 모양이 어떠한 영향을 미치는지에 대해 알아보았다. 그리고 2차 미분에 의한 변곡점을 이용하여 RI sensitivity를 향상시켰다. 셋째, host 물질로 Cucurbit[n]urils (CB[n])라는 물질을 사용하고 guest 물질로 항암제를 사용하여 항암제의 캡슐화와 방출을 CID로 측정하였다. 넷째, 각각 다른 전하량과 결합 상수를 가지는 guest 물질에 따른 CID 현상을 측정하여 전하량과 결합 상수와 CID 현상과의 상관관계에 대해 알아보았다. 이러한 RI sensitivity에 대한 금 나노 입자의 모양 효과와 RI sensitivity를 향상시킬 수 있는 방법은 LSPR 바이오 센서에 대한 응용 가능성을 넓힌다. 또한, complex를 CID에 적용한 실험 결과들은 CID에 대한 보다 높은 이해를 돕고, CID의 다양한 응용 가능성을 제시한다.

## English Abstract

Plasmonic gold nanoparticles have unique optical properties due to their localized surface plasmon resonance (LSPR) phenomena, depending on their shape, size, refractive index (RI) of the surrounding medium and so on. These gold nanoparticles have been applied in many fields because they have the advantages of being biocompatible, having high chemical stability and easy surface modification. Gold nanoparticles can be used in LSPR biosensors by spectral shifts along the refractive index of the surrounding medium, as well as changes in LSPR linewidths caused by chemical interface damping (CID) by materials attached to the surface. Based on this, there are various applications such as biosensor, drug delivery and energy fields. However, there is still a lack of information on chemical interface damping effect, and further studies at the single particle level are needed to increase the possibility of applying gold nanoparticles.

In this study, we used Scanning Electron Microscope (SEM), Dark-Field (DF) microscopy, and UV-Vis spectroscopy (UV-Vis) to analyze the optical properties of single gold nanoparticles. First, the optical properties of relatively unknown gold nanocubes (AuNCs) were examined. Second, spherical gold nanospheres (AuNSs) and AuNCs with the same size (50 nm) and the different shape were used to investigate the effect of the shape of gold nanoparticles on the RI sensitivity according to the refractive index of the surrounding medium. RI sensitivity was

improved by using the inflection point by the second derivative. Third, we measured encapsulation and release of drug by applying CID using Cucurbit[n]uril (CB[n]) as the host materials and anticancer agent as the guest materials. Fourth, the correlation between the charge amount, the binding constant and the CID phenomenon was observed by measuring the CID phenomenon according to the guest materials having each different charge amount and binding constant. The shape effect of the gold nanoparticles on the RI sensitivity and the method of improving the RI sensitivity broaden the applicability of the LSPR biosensor. In addition, the experimental results of applying the complex to CID help to better understand CID and suggest various applications of CID.

## Index

Korean Abstract .....	i
English Abstract .....	iii
Index .....	v
Figure Index .....	vii
Scheme Index .....	x
Table Index .....	xi
<b>1. Introduction</b> .....	<b>1</b>
1.1. Gold nanoparticles .....	1
1.2. Chemical Interface Damping (CID) .....	3
1.3. Inflection point of the LSPR peak .....	4
1.4. Cucurbit[n]urils (CB[n]) .....	6
<b>2. Experimental Section</b> .....	<b>8</b>
2.1. Materials .....	8
2.2. Characterization of Gold Nanoparticles .....	8
2.3. Sample Preparation for Single Particle Study .....	9
2.4. Single Particle Microscopy and Spectroscopy .....	9
<b>3. Results and Discussion</b> .....	<b>12</b>
3.1. Single-Particle Study: Plasmon Damping of Gold Nanocubes with Vertices by Adsorbate Molecules .....	12
3.2. Shape Effect on the Refractive Index Sensitivity at Localized Surface Plasmon Resonance Inflection Points of Single Gold Nanocubes with Vertices .....	18
3.3. Encapsulation-Release Identification of Guest Molecules Using Chemical Interface Damping Effect between Gold Nanoparticles and Host-Guest Complex .....	32
3.4. Correlation Between CID and Binding Constants and Charge Effect of Guest Materials .....	42

<b>4. Conclusions</b> .....	46
<b>5. References</b> .....	49

## Figure Index

- Figure 1. Chemical structure and schematic of CB[7]-NH<sub>2</sub> and CB[6]-SH. .... 7
- Figure 2. Photograph (A) and schematic (B) depicting the working principle of single particle microscopy and spectroscopy ..... 11
- Figure 3. (A) SEM image of 50-nm AuNCs with vertices. (B) UV–Vis absorption spectrum of 50-nm AuNCs in water. A LSPR extinction peak is observed at around 546 nm. .... 14
- Figure 4. (A) Single-particle scattering image of three AuNCs measured under DF microscopy. (B) Scattering spectra obtained from single AuNCs indicated by a yellow square in (A). .... 14
- Figure 5. (A) DF scattering spectra of a single AuNC at 3-min intervals after the addition of 1-decanethiol in ethanol. (B) Change in the LSPR linewidth (or FWHM) as a function of time. .... 17
- Figure 6. SEM images of AuNSs (A) and AuNCs with vertices (B). UV-Vis extinction spectrum of AuNSs (C) and AuNCs (D) dispersed in water. .... 19
- Figure 7. (A) Dark-field image of single AuNSs illuminated by white light. (B) Scattering spectra of the single AuNSs from the green square in (A). (C) Dark-field image of single AuNCs illuminated by white light. (D) Scattering spectra of the single AuNCs from the yellow square in (C). .... 21
- Figure 8. Lorentzian fitting to experimental scattering spectra of (A) AuNS and (B) AuNC with vertices. The experimental scattering spectra were well fitted to a Lorentzian function for both AuNS and AuNC with a single resonant mode. .... 23
- Figure 9. Change in the LSPR scattering spectra of single AuNS (A) and AuNC (B) in the different local RI media: air, water, oil. The scattering spectra

represent average measurements as a demonstration of the LSPR peak shift with increasing the local RI from air to oil. (C) LSPR wavelength shifts for AuNS (red) and AuNC (blue) as a function of the local RI of medium.

..... 24

Figure 10. Inflection point method for single particle LSPR scattering sensing with AuNSs in the three local refractive indexes (air, water, and oil). (A–C) LSPR scattering efficiencies (first row), and its first (second row), and second (third row) order derivatives. (D) Peak energy plotted against the three local RI for points A, B, and C. (E) Sensitivity of local RI media on peak shifts A, B and C. .... 28

Figure 11. Inflection point method for single particle LSPR scattering sensing with AuNCs in the three local refractive indexes (air, water, and oil). (A–C) LSPR scattering efficiencies (first row), and its first (second row), and second (third row) order derivatives. (D) Peak energy plotted against the three local RI for points A, B, and C. (E) Sensitivity of local RI media on peak shifts A, B and C. .... 31

Figure 12. (A) SEM image of single AuNRs with aspect ratio  $25\text{nm} \times 73\text{nm}$ . (C) Structure of oxaliplatin. UV-Vis extinction spectra of the AuNRs (B) and oxaliplatin (D) dispersed in water. .... 33

Figure 13. (A) Schematic to show CID phenomenon between AuNR and CB[7]-NH<sub>2</sub>. (B) Comparison of DF scattering spectra among single AuNRs capped by CTAB, attached with CB[7]-NH<sub>2</sub> and with complex (CB[7]-NH<sub>2</sub>@Ox-Pt). (C) Comparison of FWHM value about single AuNRs capped by CTAB, single AuNRs attached with CB[7]-NH<sub>2</sub> and attached with complex (CB[7]-NH<sub>2</sub>@Ox-Pt). .... 35

Figure 14. UV-Vis spectra of oxaliplatin, spermine and their respective complex. Intensity increase and Red shift indicate encapsulation of oxaliplatin into

CB[7]-NH <sub>2</sub> (Black, Yellow). After adding spermine into complex of oxaliplatin, disappearance of oxaliplatin peak suggests release of oxaliplatin from complex (Purple). .....	38
Figure 15. Full width at half maximum change by encapsulation and release of Ox-Pt from complex. ....	40
Figure. 16 Chemical structure of guest materials with amine group. ....	43
Figure. 17 Comparison of total experimental results. Blue squares are control experiment and red circles are encapsulation of guest materials into CB[6]-SH. The more binding constant and charge number of guest materials with amine groups increase, the more FWHM is broaden. Binding constant and charge effect increase from G4 to G1. (G1: Spermine, G2: Spermidine, G3: Butane-1,4-diammonium, G4: 1-pentylammonium) .....	44

## Scheme Index

- Scheme 1. (A) Schematic to show single-particle DF scattering measurement of AuNCs in the presence of 1-decanethiol dispersed in ethanol. (B) Schematic to show the adsorption of 1-decanethiol on the Au surface. The strong binding of thiol group (-SH) on the AuNC results in chemical interface damping. .... 16
- Scheme 2. Schematic to show sequential sample preparation to encapsulate oxaliplatin into CB[7]-NH<sub>2</sub>. .... 34
- Scheme 3. Schematic of release of Ox-Pt from complex (CB[7]-NH<sub>2</sub>@Ox-Pt). Two methods are used to induce release of Ox-Pt. One is using spermine as competitive guest materials and the other is pH changes. .... 37

## Table Index

Table 1. Local refractive index Sensitivities of single AuNSs at each point (first inflection point A, LSPR peak B, second inflection point C) .....	27
Table 2. Local refractive index Sensitivities of single AuNCs at each point (first inflection point A, LSPR peak B, second inflection point C). .....	30
Table 3. Average FWHM value(meV) depending on each attached material on the surface of single AuNRs. ....	41
Table 4. Average FWHM value(meV) depending on each attached material on the surface of single AuNRs. (G1: Spermine, G2: Spermidine, G3: Butane-1,4-diammonium, G4: 1-pentylammonium) .....	45

# 1. Introduction

## 1.1 Gold nanoparticles

Plasmonic gold nanoparticles (AuNPs) have unique optical properties that depend on their shapes and sizes, and on the refractive index (RI) of the surrounding media. These properties are induced by the localized surface plasmon resonance (LSPR) effect.<sup>1-3</sup> When gold nanoparticles are irradiated, the conduction electrons on their surfaces are excited and collectively oscillate with the incident electromagnetic field. Furthermore, the strong interaction between gold nanoparticles causes light to be confined into sub-diffraction volumes.<sup>4</sup> For many years, the optical properties of single AuNPs have been intensively investigated by far-field single particle imaging and spectroscopic techniques, such as scattering-based dark-field microscopy<sup>5</sup> and absorption-based photothermal imaging<sup>6,7</sup>, without ensemble averaging. It has been reported that the LSPR of AuNPs is strongly dependent on the three-dimensional (3D) structure and size of the nanoparticles<sup>2</sup>, as well as on the RI of the surrounding medium.<sup>8</sup> Accordingly, by controlling these parameters, it is possible to tune the characteristic plasmonic properties for specific purposes and applications.<sup>3, 9</sup> Furthermore, the AuNPs have unique intrinsic properties<sup>8</sup>, such as biocompatibility<sup>10</sup>, high chemical stability<sup>11</sup>, convenient surface modification with organic and biological molecules<sup>12, 13</sup>, etc. The many advantages of AuNPs has thus led to their use in LSPR-based biosensors<sup>14, 15</sup>. The conventional LSPR biosensors are based on

AuNPs functionalized with receptors that confer specific binding abilities for target molecules, then the LSPR peak is shifted and dampened upon the attachment of the target molecules on the nanoparticle surface<sup>16</sup>. Thus, the LSPR changes of AuNPs is monitored by the shift of the peak maximum as well as broadening of the peaks<sup>17</sup>; such changes indicate the presence of target molecules.<sup>18</sup>

Gold nanoparticles with edges and vertices, including gold nanocubes (AuNCs), have gained great attention as plasmonic biosensors due to their characteristic structure dependent optical properties resulting from localized surface plasmon resonance (LSPR), which refers to the collective oscillation of free electrons in the conduction band induced by incident light of a specific wavelength.<sup>19-21</sup> In recent studies, it was found that AuNCs with vertices exhibit stronger LSPR effects than spherical nanoparticles over a wider energy range. Furthermore, AuNCs have been used as a LSPR biosensor with high sensitivity and selectivity for cancer relevant microRNA biomarker.<sup>19</sup>

Despite the recent studies on CID in gold nanoparticles, there have been no studies to describe the chemical effect in single AuNCs and our understanding is very limited. In this respect, it is of importance to carry out single nanoparticle scattering studies to provide deeper insight into plasmon damping caused by molecules adsorbed onto the surface of AuNCs. In the present study, we report single-particle dark-field (DF) studies to elucidate the characteristic scattering properties of 50-nm AuNCs. Furthermore, we demonstrate plasmon damping induced by thiolate molecules adsorbed onto the surface of AuNCs with edges and vertices. We then

disclose a single-particle study to monitor real-time binding events of 1-decanethiol in ethanol on single AuNCs.

## 1.2 Chemical Interface Damping (CID)

Surface plasmon damping (or dephasing) is a very interesting optical property that arises in gold nanoparticles. Mechanisms for surface plasmon damping include bulk metal damping ( $\Gamma_{\text{bulk}}$ ), radiation damping ( $\Gamma_{\text{rad}}$ ), electron-surface scattering ( $\Gamma_{\text{surf}}$ ), and chemical interface damping (CID) ( $\Gamma_{\text{CID}}$ )<sup>22</sup> Therefore, the LSPR total damping channel can be described by the following equation (1).

$$\Gamma_{\text{tot}} = \Gamma_{\text{bulk}} + \Gamma_{\text{rad}} + \Gamma_{\text{surf}} + \Gamma_{\text{CID}} \quad (1)$$

Among the various decay mechanisms, CID is a recently proposed damping channel pathway, which directly transfers interfacial hot-electron energy from metals to a chemical material conjugated on the metal surface.<sup>23</sup> In CID, the presence of closely or strongly interacting adsorbate molecules induces the direct transfer of plasmon-induced hot-electrons to the adsorbates' empty orbitals (LUMOs: lowest unoccupied molecular orbitals).<sup>24</sup> To date, single-particle scattering microscopy and spectroscopy have mainly been adopted for elucidating plasmon damping mechanisms in single gold nanoparticles with different three-dimensional (3D) structures.<sup>22, 25</sup> Homogeneous LSPR linewidth measurements, using only single

nanoparticles over the heterogeneous linewidth of an ensemble spectrum, have provided an unprecedented technique to overcome the time scale limitation present in ultrafast spectroscopy techniques. However, despite the various recent studies about CID using single particle spectroscopy, application information about the CID and our understanding on its mechanism in plasmonic gold nanoparticles are limited. Therefore, application study of CID by using host-guest chemistry is carried out in this paper. Because anticancer drugs and overexpressed anticancer biomarkers were used as guest materials, it is possible to apply to various fields such as drug delivery, cancer therapy, thermotherapy.

### **1.3 Inflection point of the LSPR peak**

Despite the remarkable advantages of LSPR-based biosensors, they still have many fundamental limitations. First, the efficiency of LSPR-based sensor using AuNPs is low in comparison with surface plasmon polariton (SPP) sensors.<sup>26</sup> The accurate determination of LSPR properties is affected by a realistic representation of the wavelength-dependent dielectric function of the nanoparticles.<sup>27</sup> Therefore, simplistic models negatively impact the fundamental quantities that are necessary for the reliable fabrication of plasmonic devices.<sup>28</sup> Second, LSPR biosensors are limited by the unsymmetrical broadening of LSPR peaks when measuring the changes in the local environment at the nanoparticle surface.<sup>29</sup> It should also be noted that

alterations in the shape of the LSPR peak can have a negative effect on the sensing efficiency.<sup>30</sup> To overcome these limitations, recent studies have, for example, improved the effectiveness by using lithographic methods, but there are some disadvantages such as the high processing cost and low yield.<sup>26</sup> Recently, Chen and co-workers reported a different approach that evaluates the changes in LSPR curvature of ensemble samples with respect to RI changes.<sup>26</sup> They showed that higher RI sensitivity was obtained in the inflection points (IFs) located at the long wavelength side (or low energy side) of the LSPR extinction peak.<sup>29</sup> However, that report was based on only ensemble samples of Au nanoparticles rather than single nanoparticles. Very recently, a single particle study on homogeneous LSPR IFs of single Au bipyramids was reported, however, our understanding of the effect of the NPs shape on the RI sensitivity at LSPR IFs of single Au nanoparticles is still scarce.<sup>31</sup> In this study, we carried out single particle studies to evaluate the shape-dependent RI sensitivity at LSPR IFs of homogeneous scattering spectra experimentally measured for gold nanospheres (AuNSs) and gold nanocubes (AuNCs), to compare structures with and without vertices. We investigated the LSPR sensing effect of single AuNSs and AuNCs deposited on a glass slide with three different surrounding media of known RI values (air, water, and oil). The results indicate that tracking the homogeneous LSPR IFs of AuNCs with vertices can be effectively used to develop LSPR-based biosensors with high RI sensitivity.

## 1.4 Cucurbit[n]urils (CB[n])

Cucurbit[n]urils (CB[n]) are macrocycles with n glycoluril units ( $n = 5-8$ ).<sup>32</sup> A cavity of CB[n] is composed of two hydrophilic carbonyl-lined portals capping a central hydrophobic cavity.<sup>34</sup> Among various CB[n] sizes, CB[7] is water-soluble macrocycles and has good solubility in water and strong affinity with many kinds of guest materials. A variety of organic drugs and biologically relevant materials can be encapsulated into CB[n].<sup>33, 35</sup> In this paper, oxaliplatin which is clinical antitumor drugs but has high cytotoxicity to normal cells was used as guest molecules.<sup>36, 37</sup> Oxaliplatin has been proved to be capable of binding to CB[7] with considerable binding affinity. Host-guest complex of CB[7]@oxaliplatin can have low cytotoxicity than just oxaliplatin.<sup>36</sup> In this study, we used CB[7]-NH<sub>2</sub> to attach more efficiently on the surface of AuNRs.

In case of CB[6], CB[6] has the poor solubility in common solvents including water than CB[7] so is difficult to study the host-guest complex chemistry in solution.<sup>32</sup> However, CB[6]-SH was used in this study. CB[6]-SH has more solubility in common solvents than CB[6]. CB[6] has a fairly high binding affinity about the n-alkylammonium ions and  $\alpha,\omega$ -alkanediammonium ions.<sup>38</sup> In this paper, spermine tetrahydrochloride, spermidine trihydrochloride, 1,4-diaminobutane dihydrochloride, n-pentyl ammonium chloride were used as guest materials<sup>38</sup> to study relationship between binding constant and + charge number and CID of guest materials. Figure 1 shows chemical structure of CB[7]-NH<sub>2</sub> and CB[6]-SH.

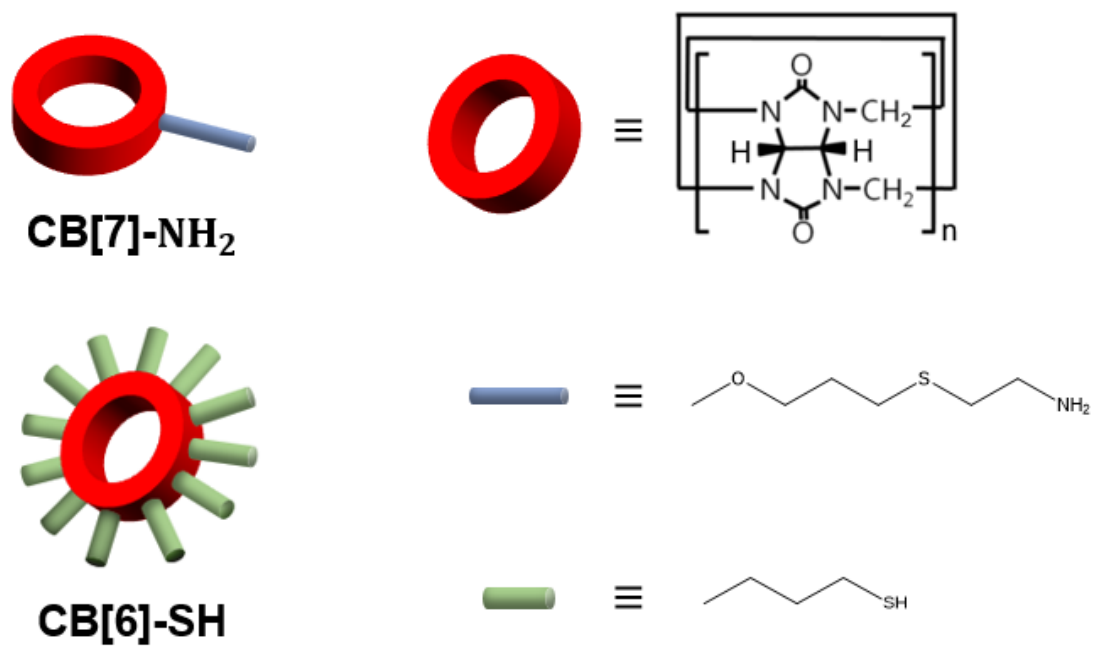


**Fig. 1** Chemical structure and schematic of CB[7]-NH<sub>2</sub> and CB[6]-SH.

## **2. Experimental Section**

### **2.1. Materials**

Cetyltrimethylammonium bromide (CTAB)-stabilized gold nanospheres (AuNSs) and gold nanocubes (AuNCs) with an average size of 50 nm were purchased from Nanopartz (Loveland, CO, USA). Citrate-stabilized gold nanorods (AuNRs) with ARs (25 nm × 73 nm) were purchased from Nanopartz (Loveland, CO, USA). 1-decanethiol used in this study was purchased from Sigma-Aldrich (St. Louis, MO, USA). All cucurbit[n]urils (CB[7]-NH<sub>2</sub>, CB[6]-SH) and some guest materials (spermine, spermidine, Butane-1,4-diammonium, 1-pentylammonium) were provided from Professor Kim Ki-Moon Laboratory of POSTECH. Oxaliplatin and cisplatin were purchased from Sigma-Aldrich (St. Louis, MO, USA). Immersion oil was purchased from Sigma-Aldrich (St. Louis, MO, USA).

### **2.2. Characterization of Gold Nanoparticles**

The structural characterization of AuNSs, AuNCs and AuNRs was conducted by scanning electron microscopy (SEM, JSM-6500, JEOL, Japan) to assess the shapes and sizes. Furthermore, the LSPR absorption spectra of the AuNSs, AuNCs and AuNRs dispersed in water were measured using a Varian Carry 300 UV-Vis spectrophotometer (Agilent, USA).

### **2.3. Sample Preparation for Single Particle Study**

Microscope coverglasses were cleaned by first sonicating in ethanol for 15 min, secondly in acetone for 15 min, finally sonicating in ethanol for 15 min and then followed by O<sub>2</sub> plasma cleaning for 30 seconds. The preparation of the samples was simple. First, the colloid solution was diluted with distilled water to lower the concentration. The diluted solution was sonicated for 10 min at room temperature and was then dropped on a washed slide glass and covered with a 22 mm × 22 mm No. 1.5 cover glass (Corning, NY). To achieve the conditions of air as surrounding medium, the aqueous solution on the slide glass was dried after placing the cover glass. When using the oil as surrounding medium, the same procedure was followed and then, after drying the aqueous solution, the immersion oil was added. The concentration of Au nanoparticles deposited on the glass slide was adjusted to be approximately 1 μm<sup>-2</sup> in order to facilitate the measurement of a single particle characterization and to minimize inter-particle LSPR coupling resulting in a spectral shift.

### **2.4. Single particle microscopy and spectroscopy**

We performed scattering-based dark-field (DF) microscopy using an inverted microscope (ECLIPSE Ti-U, NIKON, Japan). In the DF mode, we used a Nikon Plan

Fluor oil iris objective (100×) with an adjustable numerical aperture (NA, 0.5–1.3) and a Nikon DF condenser for DF imaging. To obtain DF scattering images with high quality, we used an Andor EMCCD camera (iXon Ultra 897, UK). We analyzed the collected DF images with the Image J software. Furthermore, single particle spectra of AuNSs and AuNCs were taken by using an Andor spectrometer (SHAMROCK303i, SR-303I-A, UK) equipped with an Andor CCD camera (Newton DU920P-OE, UK). We collected the scattered light from AuNPs by an objective lens and sent to the entrance of the spectrometer for taking a spectrum. The scattered light was then dispersed by a grating (300 l/mm) inside the spectrometer and detected by the Andor CCD camera (Newton DU920P-OE, UK). We obtained a background spectrum at an area without nanoparticles. Finally, Matlab programs specially designed for this study were used to perform data analysis and to obtain single particle spectra.

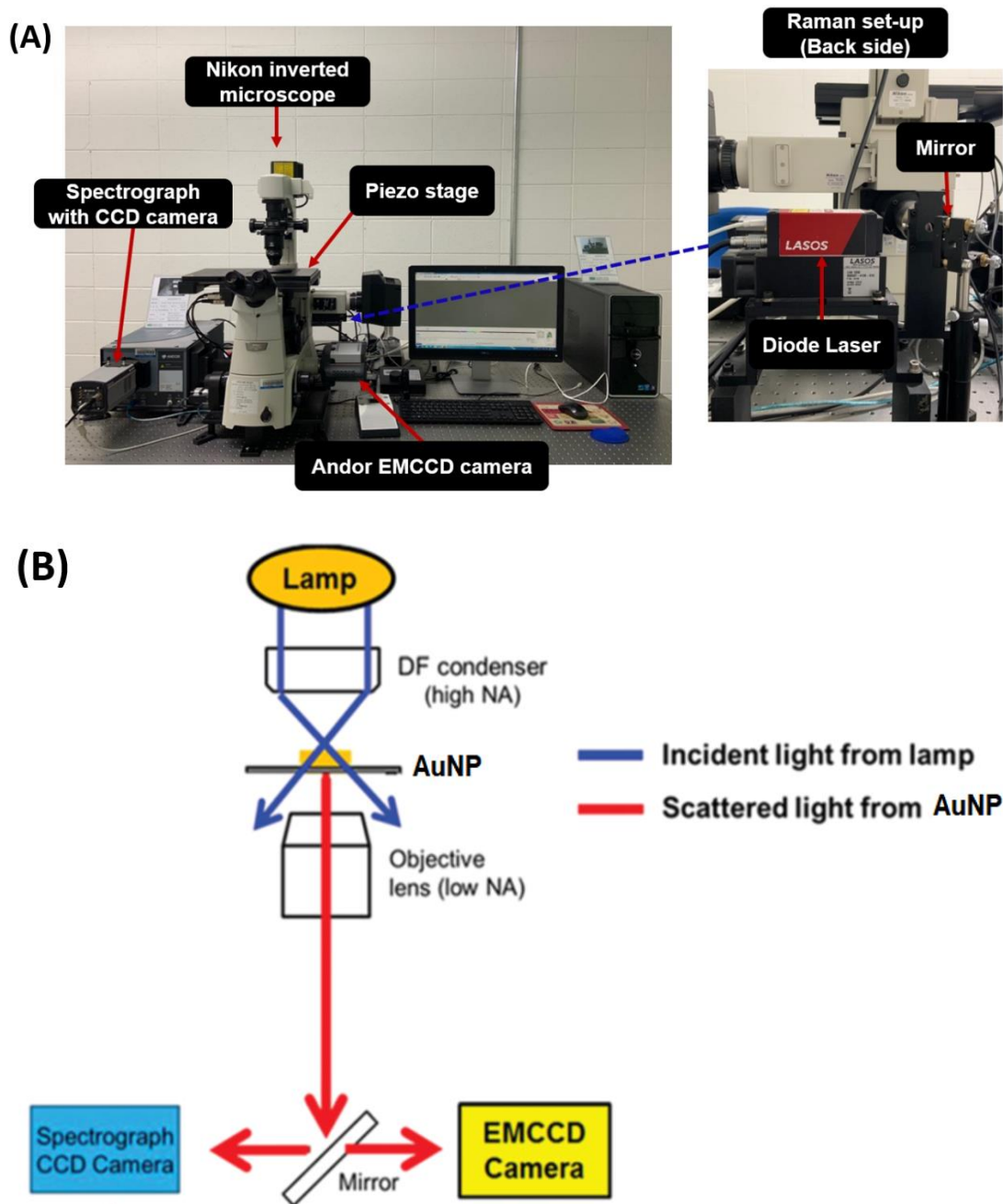


**Fig. 2** Photograph (A) and schematic (B) depicting the working principle of single particle microscopy and spectroscopy

### 3. Results and Discussion

#### 3.1. Single-Particle Study: Plasmon Damping of Gold Nanocubes with Vertices by Adsorbate Molecules

We report single-particle dark-field (DF) studies to elucidate the characteristic scattering properties of 50-nm AuNCs. Furthermore, we demonstrate plasmon damping induced by thiolate molecules adsorbed onto the surface of AuNCs with edges and vertices. We then disclose a single-particle study to monitor real-time binding events of 1-decanethiol in ethanol on single AuNCs. For this experiment, AuNCs capped with cetyltrimethylammonium bromide (CTAB) were purchased from Nano-Seedz (Ma On Shan, Hong Kong). An average diameter of AuNCs was determined to be about 50 nm by field emission-scanning electron microscopy (FE-SEM) (Figure 3(A)). The ensemble absorption spectrum of AuNCs in water was measured with a Varian Cary (Sydney, Australia) 300 UV–Vis spectrophotometer (Figure 3(B)). For AuNCs, the LSPR wavelength was observed at around 546 nm as seen in Figure 3(B). However, it was challenging to obtain detailed information on the characteristic scattering properties and surface plasmon damping in single AuNCs from the ensemble measurement. In this respect, single-particle studies were required to deepen our understanding of their unique scattering properties as well as the CID effect without ensemble averaging. We employed single-particle scattering studies to reveal the scattering properties of single AuNCs in DF microscopy and spectroscopy (Figure 2). Figure 4(A) shows a DF scattering image of single AuNCs,

while Figure 4(B) shows the single-particle scattering spectra of AuNCs highlighted within the yellow square in Figure 4(A). A LSPR peak was observed at around 560 nm for AuNCs, which is in a good agreement with the ensemble spectrum in Figure 3(B).

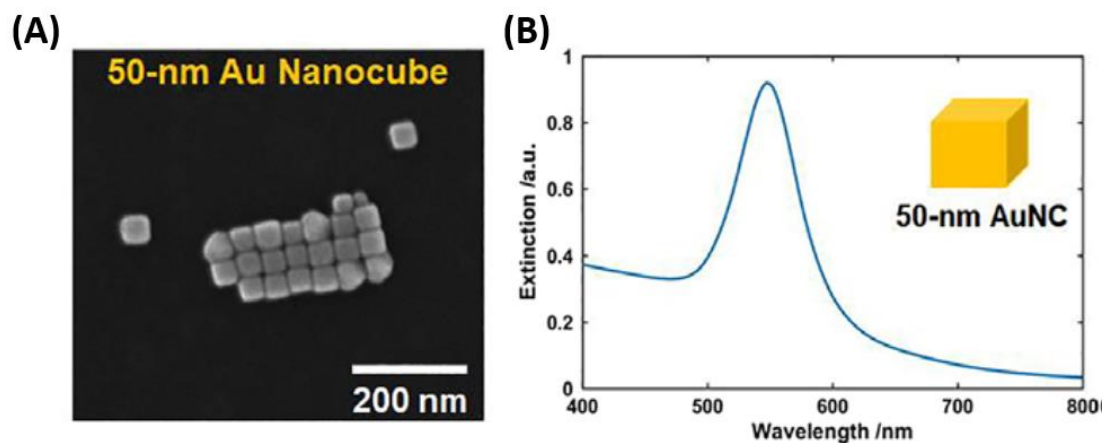


**Fig. 3** (A) SEM image of 50-nm AuNCs with vertices. (B) UV-Vis absorption spectrum of 50-nm AuNCs in water. A LSPR extinction peak is observed at around 546 nm.

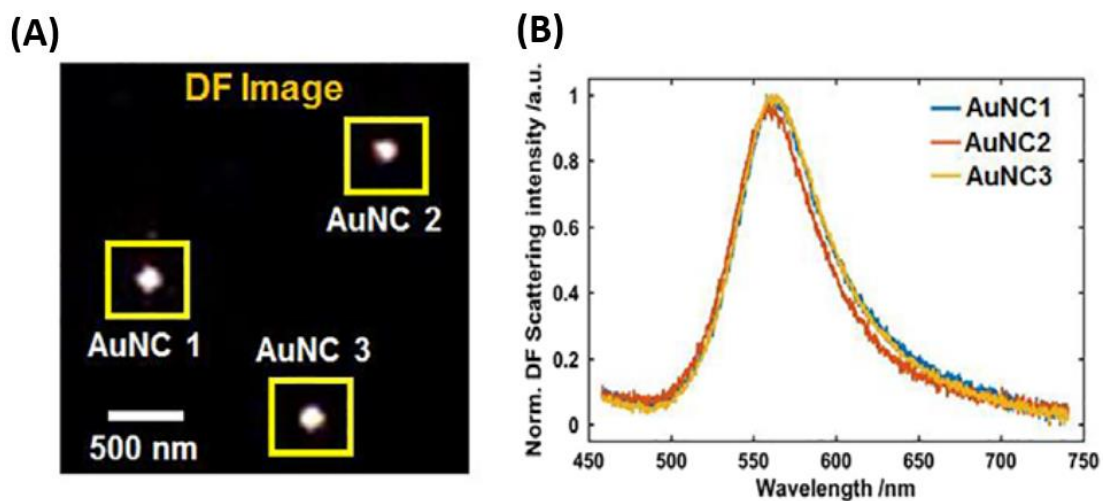
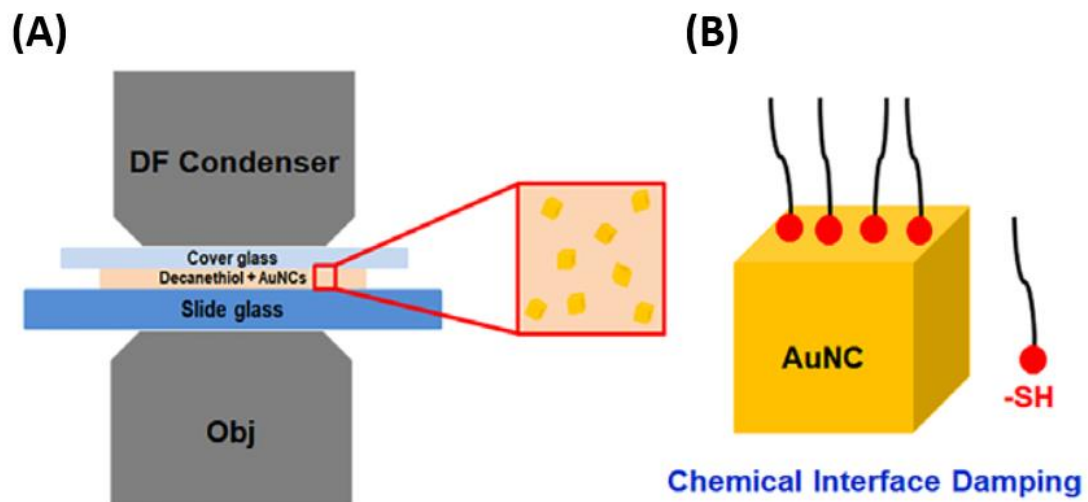


**Fig. 4** (A) Single-particle scattering image of three AuNCs measured under DF microscopy. (B) Scattering spectra obtained from single AuNCs indicated by a yellow square in (A).

We then carried out a real-time study to monitor the binding events of thiol molecules (1-decanethiol in ethanol) onto single AuNCs to investigate the CID effect under DF microscopy and spectroscopy (Scheme 1). As shown in Scheme 1(B), thiol molecules strongly adsorbed onto the gold surfaces through the formation of strong covalent bonds between gold and sulfur.<sup>39-41</sup> Next, the attached thiol molecules reorganized on the gold surface into monolayers with high density, and the carbon chains of 1-decanethiol interact with each other through attractive van der Waals forces.<sup>42</sup> In this study, the DF scattering spectra of single AuNCs with vertices were obtained at 3-min intervals after introducing 1  $\mu$ M 1-decanethiol (Figure 5(A)). As shown in Figure 5(A), we observed a decrease in the DF scattering intensity after the strong attachment of 1-decanethiol on the gold surface. More importantly, the homogeneous LSPR linewidth of single AuNCs was broadened over time due to the CID effect (Figures 5(A)). The result can be ascribed to the adsorption effect on single AuNCs upon introduction of 1-decanethiol. Figure 5(B) presents the change of the LSPR linewidth in single AuNCs with respect to time after injecting 1  $\mu$ M 1-decanethiol in ethanol. As seen in Figure 5, the adsorption of thiolate molecules led to a strong decrease in the scattering intensity as a function of time. To the best of the author's knowledge, this is the first report to describe a single-particle study on the chemical damping effect in AuNCs with edges and vertices.



**Scheme 1.** (A) Schematic to show single-particle DF scattering measurement of AuNCs in the presence of 1-decanethiol dispersed in ethanol. (B) Schematic to show the adsorption of 1-decanethiol on the Au surface. The strong binding of thiol group (-SH) on the AuNC results in chemical interface damping.

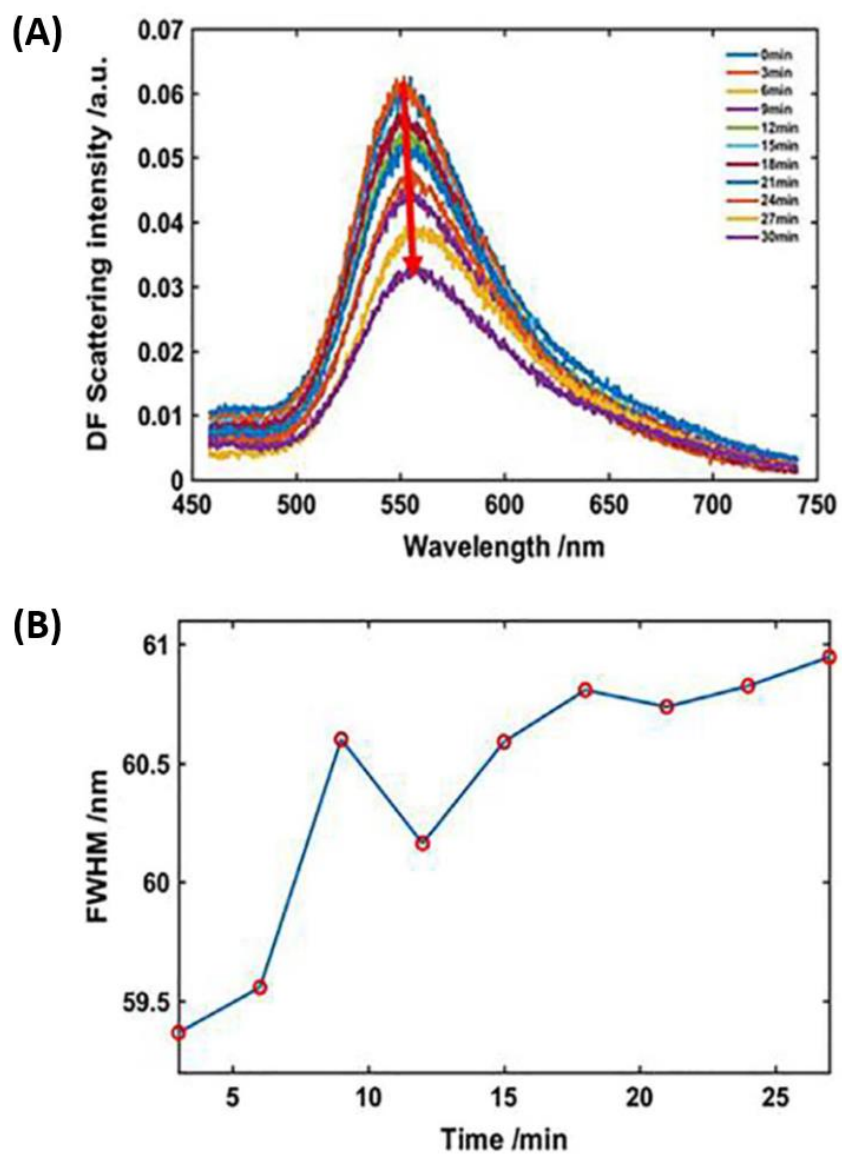


**Fig. 5** (A) DF scattering spectra of a single AuNC at 3-min intervals after the addition of 1-decanethiol in ethanol. (B) Change in the LSPR linewidth (or FWHM) as a function of time.

### **3.2. Shape Effect on the Refractive Index Sensitivity at Localized Surface Plasmon Resonance Inflection Points of Single Gold Nanocubes with Vertices**

The size and shape of AuNSs and AuNCs was characterized by SEM. Figure 6A, B show the SEM images of AuNSs (A) and AuNCs with vertices (B), with average sizes of 50.3 ( $\pm 1.7$ ) nm and 51.1 ( $\pm 2.1$ ) nm, respectively. The size of 51.1 nm in AuNC indicates the length of one side of cube. The extinction spectra of both AuNSs (Fig. 6C) and AuNCs (Fig. 6D) was then obtained with a Varian Cary 300 UV-Vis spectrophotometer. We found that the extinction spectra obtained from AuNSs and AuNCs were very similar. However, the LSPR peak was seen at around 535 nm for AuNSs, while the LSPR peak was observed at approximately 547 nm for AuNCs dispersed in water. Furthermore, the LSPR linewidth was different for the AuNSs and AuNCs. In Fig. 6, the measurements at the ensemble level are limited by heterogeneity issues and, hence, single particle measurements are required for a better understanding on their optical properties.

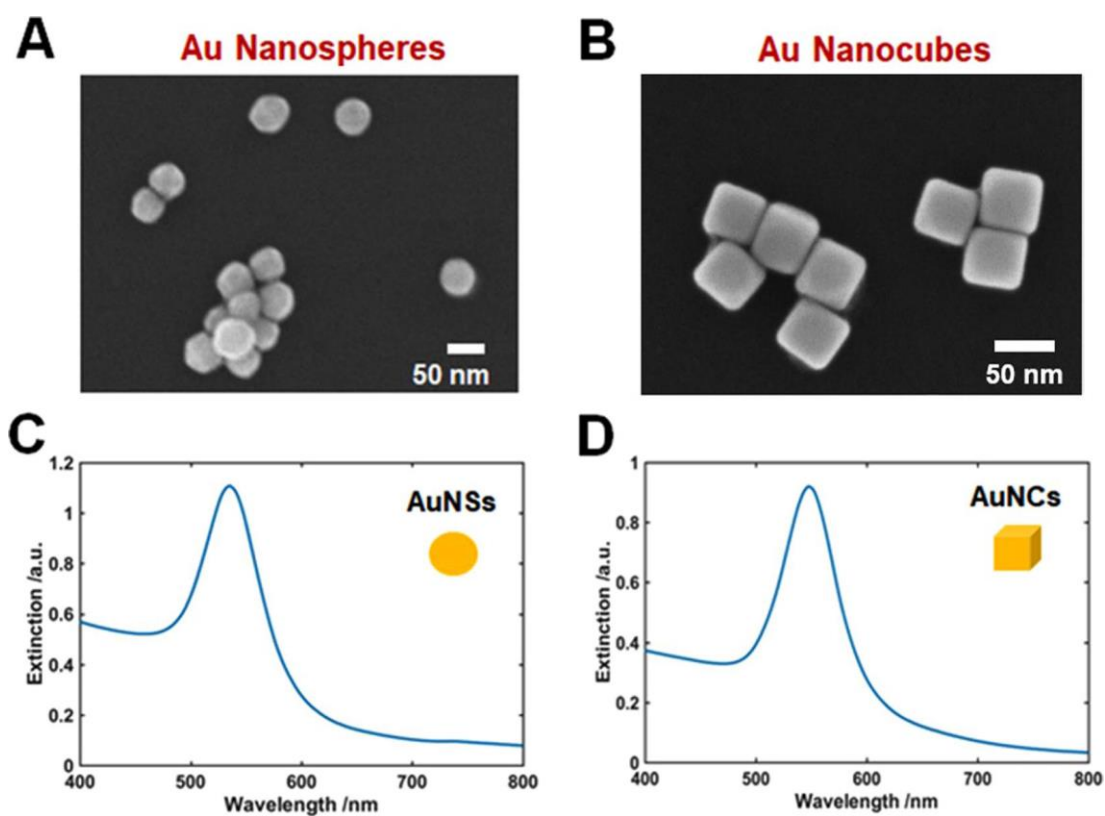


**Fig. 6** SEM images of AuNSs (A) and AuNCs with vertices (B). UV-Vis extinction spectrum of AuNSs (C) and AuNCs (D) dispersed in water.

Scattering-based DF microscopy and spectroscopy was used to characterize the shape-dependent optical properties of AuNSs and AuNCs with vertices at the single particle level.<sup>43</sup> The experimental setup for single particle DF microscopy and spectroscopy is shown in Fig. 1. The sample was prepared by drop casting aqueous solutions of the Au nanoparticles on a pre-cleaned glass slide for DF scattering measurements. The prepared samples were then measured by illuminating with randomly-polarized white light tightly focused by a high NA oil condenser. Only the light scattered from the sample is collected by the objective lens under scattering-based DF microscopy and spectroscopy. Figure 7A shows a DF scattering image of single AuNSs with an average size of 50.3 nm. In addition, the corresponding scattering spectra of three AuNSs, indicated by a green square in Fig. 7A, are presented in Fig. 7B. It can be observed that the single particle scattering spectra of AuNSs in water had a single broad LSPR peak at around 547 nm, which was further supported by the scattering spectra of more AuNSs. Moreover, Fig. 7C presents the DF scattering image of single AuNCs with an average size of 51.1 nm, and single AuNCs with vertices also exhibited a single broad LSPR peak at around 567 nm (Figs 7D). It is worth noting that AuNCs with vertices and AuNSs of similar size showed very similar single broad LSPR peaks in their scattering spectra. Furthermore, their LSPR peak shapes are not symmetrical.

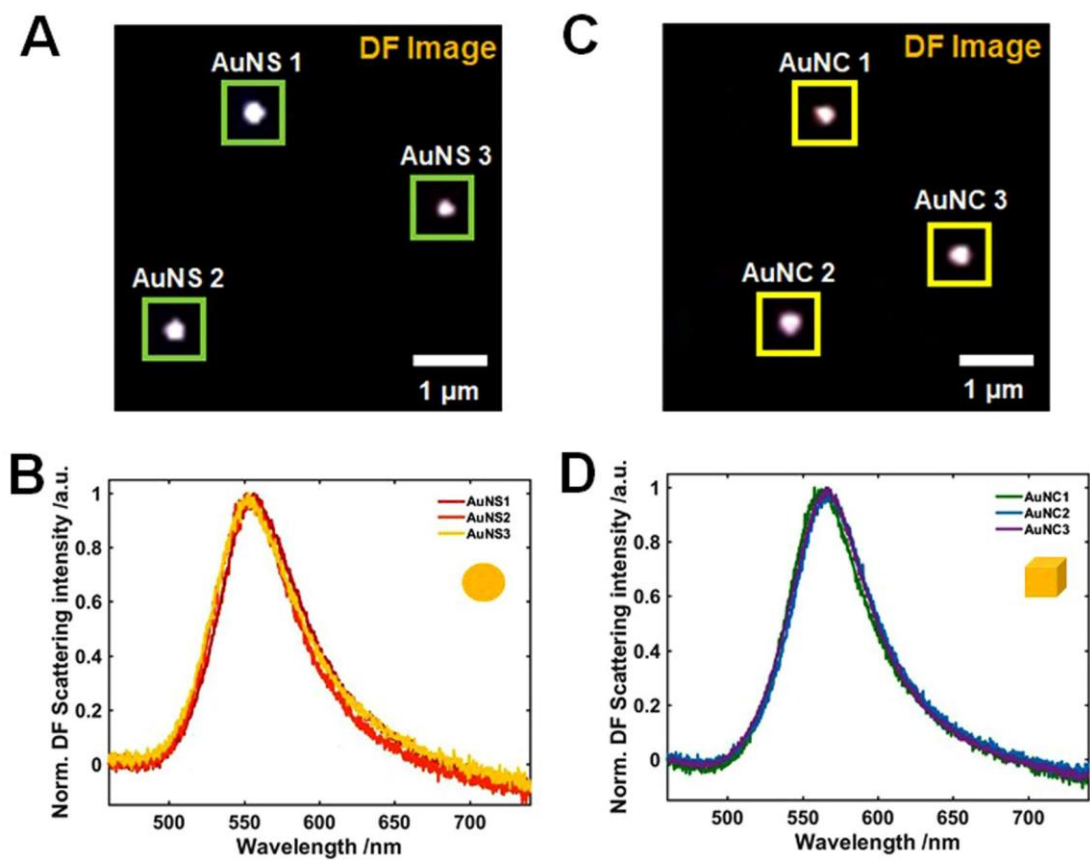


**Fig. 7** (A) Dark-field image of single AuNSs illuminated by white light. (B) Scattering spectra of the single AuNSs from the green square in (A). (C) Dark-field image of single AuNCs illuminated by white light. (D) Scattering spectra of the single AuNCs from the yellow square in (C).

To better understand the shape- and environment-dependent characteristic optical properties, the effect of changing the surrounding medium RI on the LSPR wavelength was further investigated. Therefore, the scattering spectra of single AuNSs and AuNCs were obtained in three different RI environments: air, water, and oil. Figure 8A presents the single particle scattering spectra of an AuNS fixed on a glass slide and surrounded by air, water, or oil. The LSPR spectrum was then fitted to a Lorentzian function to obtain the values of LSPR wavelength and linewidth (Fig. 8). As seen in this Fig. 8, the scattering spectra of single AuNS and AuNC were well fitted with the Lorentzian function. Figure 9A,B demonstrate that the LSPR wavelengths of both AuNS and AuNC increased as the RI increased from air to oil, which is consistent with previous studies.<sup>7, 31</sup> Fig. 9C shows a comparison of the LSPR wavelength shifts as a function of RI of surrounding medium for AuNSs (red-curve) and AuNCs with vertices (blue-curve). Single AuNCs with sharp vertices showed a higher LSPR wavelength shift and RI sensitivity than spherical AuNSs of similar size. This indicates that single AuNCs with vertices could provide a higher RI sensitivity in the development of conventional LSPR sensors.

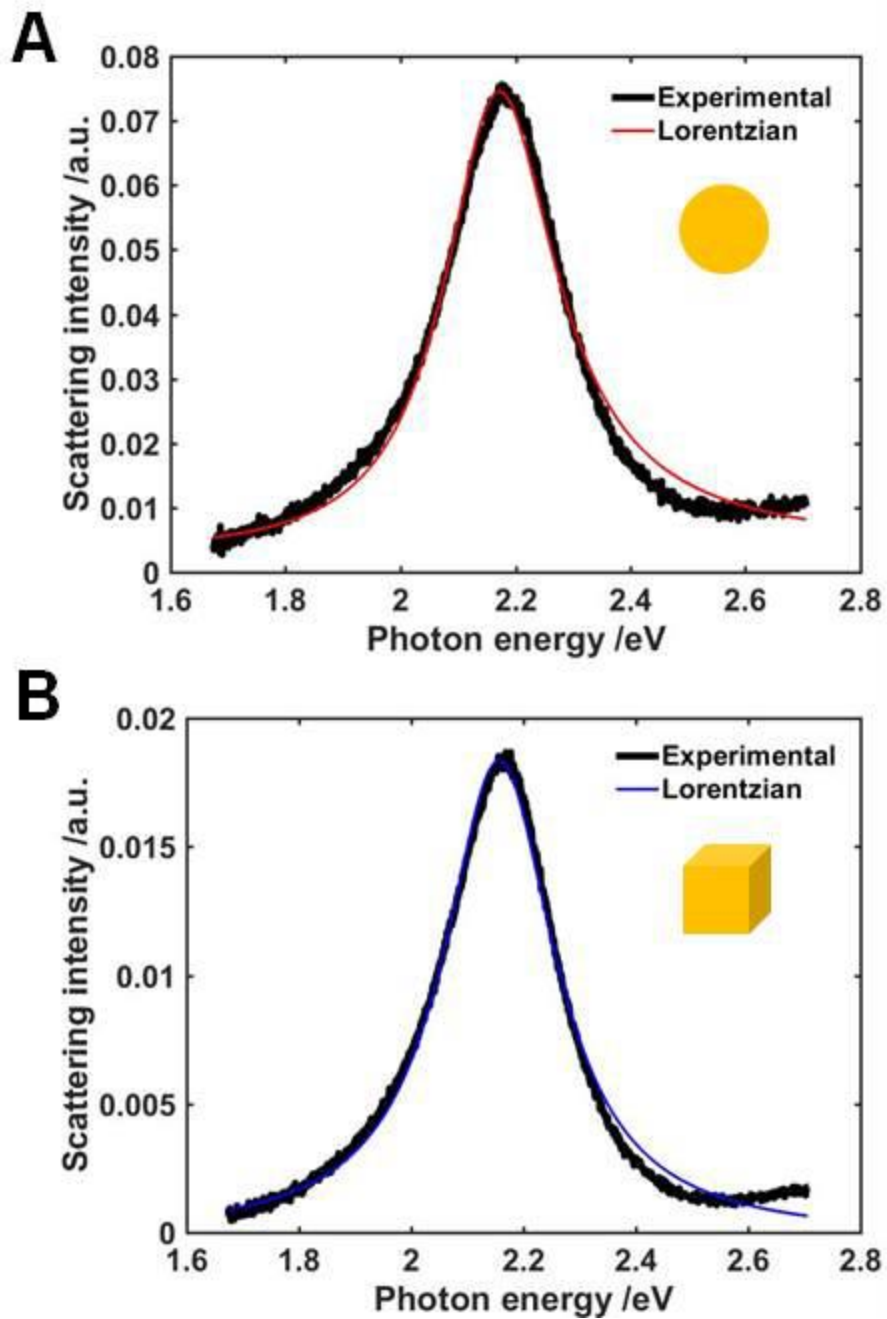


**Fig. 8** Lorentzian fitting to experimental scattering spectra of (A) AuNS and (B) AuNC with vertices. The experimental scattering spectra were well fitted to a Lorentzian function for both AuNS and AuNC with a single resonant mode.

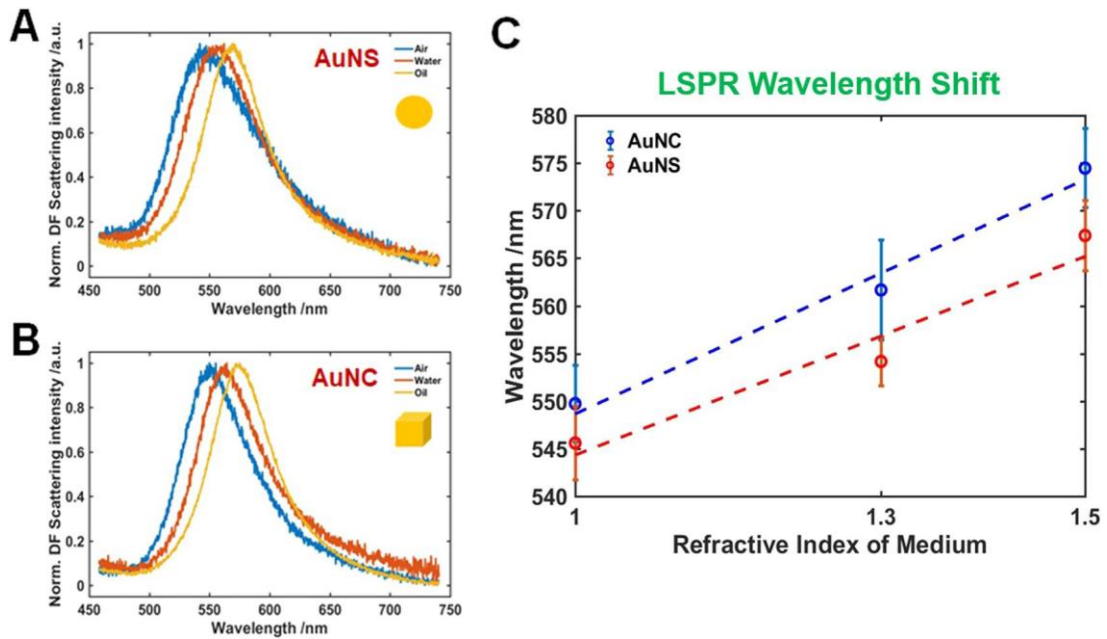


**Fig. 9** Change in the LSPR scattering spectra of single AuNS (A) and AuNC (B) in the different local RI media: air, water, oil. The scattering spectra represent average measurements as a demonstration of the LSPR peak shift with increasing the local RI from air to oil. (C) LSPR wavelength shifts for AuNS (red) and AuNC (blue) as a function of the local RI of medium.

Homogeneous LSPR inflection points (IFs, e.g., the long wavelength side) have been reported to have a higher RI sensitivity than the LSPR wavelength maximum peak in single Au bipyramids with sharp tips.<sup>31</sup> However, it is necessary to deepen our understanding on the RI sensitivity of homogeneous LSPR IFs of various Au nanoparticles with different shapes, such as multiple sharp branches, vertices, etc. We therefore investigated the shape-dependent RI sensitivity of LSPR IFs in the homogeneous scattering spectra of both AuNSs and AuNCs. The first and second derivatives of the scattering spectra taken from DF experiments were obtained using a convenient method based on the Lorentzian fitting curve function.<sup>31</sup> The first, second, and third rows in Fig. 10A–C show the scattering spectra of single AuNS and the corresponding first and second order derivatives, respectively. Each column corresponds to one of the three local RI media used (air, water, and oil). The maxima of the LSPR scattering peak, indicated as B, are located at 2.236, 2.194, and 2.170 eV for the three-different RI environments (air, water, and oil). Moreover, the local maxima and minima of the first order derivatives, A and C, are located at 2.137 and 2.335, 2.126 and 2.270, and 2.104 eV and 2.241 eV for air, water, and oil, respectively. Consequently, A and C represent the two LSPR IFs, yielding the zero values of the second order derivatives of the LSPR scattering spectra (third row). It is worth noting that the LSPR IFs coincide with the local maxima/minima of the first order derivatives and appear at the same points of A and C on the axis corresponding to photon energy for the three different RI media. As observed in the first order derivative, B appears to be the critical point of the LSPR scattering spectra of AuNS,

which indicates the zero values of the first order derivative spectra. As shown in Fig. 10, the characteristic shapes of the LSPR scattering spectra of single AuNSs in the first and second order derivatives are consistent with a previous report on LSPR IFs obtained from the extinction spectra of gold nanoparticles measured at the ensemble level.<sup>29</sup> Furthermore, the zero values of the first order derivatives axis are exactly at the point B (LSPR peak maxima), which is the point of symmetry for the three local RI media. When analyzing the curvatures, it was found that the LSPR scattering curves and second order derivatives are even functions and symmetrical to the axis of intensity, while the first order derivative curves are odd functions and are symmetrical to the axis of photon energy. The LSPR scattering spectra of 10 more AuNSs for each local RI environment were obtained and analyzed to confirm the reproducibility and consistency with the experimental results (Fig. 10). The experimental data was consistent for all the AuNSs evaluated, yielding LSPR peak maxima (B) of 2.228 ( $\pm 0.043$ ), 2.185 ( $\pm 0.034$ ), and 2.168 ( $\pm 0.019$ ) eV for the local air, water, and oil media. The LSPR IFs values, (A) and (C), were 2.127 ( $\pm 0.029$ ) and 2.329 ( $\pm 0.057$ ), 2.109 ( $\pm 0.032$ ) and 2.267 ( $\pm 0.038$ ), and 2.099 ( $\pm 0.019$ ) and 2.242 ( $\pm 0.020$ ) eV, respectively. Furthermore, considering the regime relevant to sensing properties, in which the peak energies should be approximately linear functions of the local RI media<sup>44</sup>, the linearity of the A, B, and C peak energies was examined for air, water, and oil. Figure 10D shows the plots of the energy peaks A,

B, and C against local air, water, and oil media with corresponding RI values of 1.00, 1.33, and 1.52. As seen in the Fig., the relationship between the peak energies at A, B, and C and the local RI media was linear. The slopes, determined from a fitting function, were  $0.064 \text{ eV}\cdot\text{RIU}^{-1}$  ( $R^2 = 0.9398$ ) for peak A,  $0.133 \text{ eV}\cdot\text{RIU}^{-1}$  ( $R^2 = 0.9983$ ) for B, and  $0.190 \text{ eV}\cdot\text{RIU}^{-1}$  ( $R^2 = 0.9895$ ) for C. It should be noted that the inflection point C exhibited the highest sensitivity with respect to A and the LSPR peak maxima (B), as shown in Fig. 10E. Further details are provided in the Table 1. Interestingly, the local RI sensitivity at inflection point C was improved by 5.00% compared to that at the LSPR peak maximum (B). This is consistent with previous reports using gold ensembles and single Au bipyramids for the utilization of LSPR IFs to enhance RI sensitivity.<sup>26, 29, 31</sup>

Single AuNSs	1	2	3	4	5	6	7	8	9	10	Ave	Std
Slope at inflection A ( $\text{eV}\cdot\text{RIU}^{-1}$ )	0.131	0.126	0.060	0.029	0.099	0.098	0.147	0.008	0.028	0.107	0.083	0.049
Slope at LSPR B ( $\text{eV}\cdot\text{RIU}^{-1}$ )	0.235	0.198	0.118	0.137	0.192	0.189	0.237	0.014	0.019	0.075	0.141	0.083
Slope at inflection C ( $\text{eV}\cdot\text{RIU}^{-1}$ )	0.331	0.254	0.159	0.225	0.268	0.261	0.307	0.025	0.024	0.054	0.191	0.117

**Table 1.** Local refractive index Sensitivities of single AuNSs at each point (first inflection point A, LSPR peak B, second inflection point C)

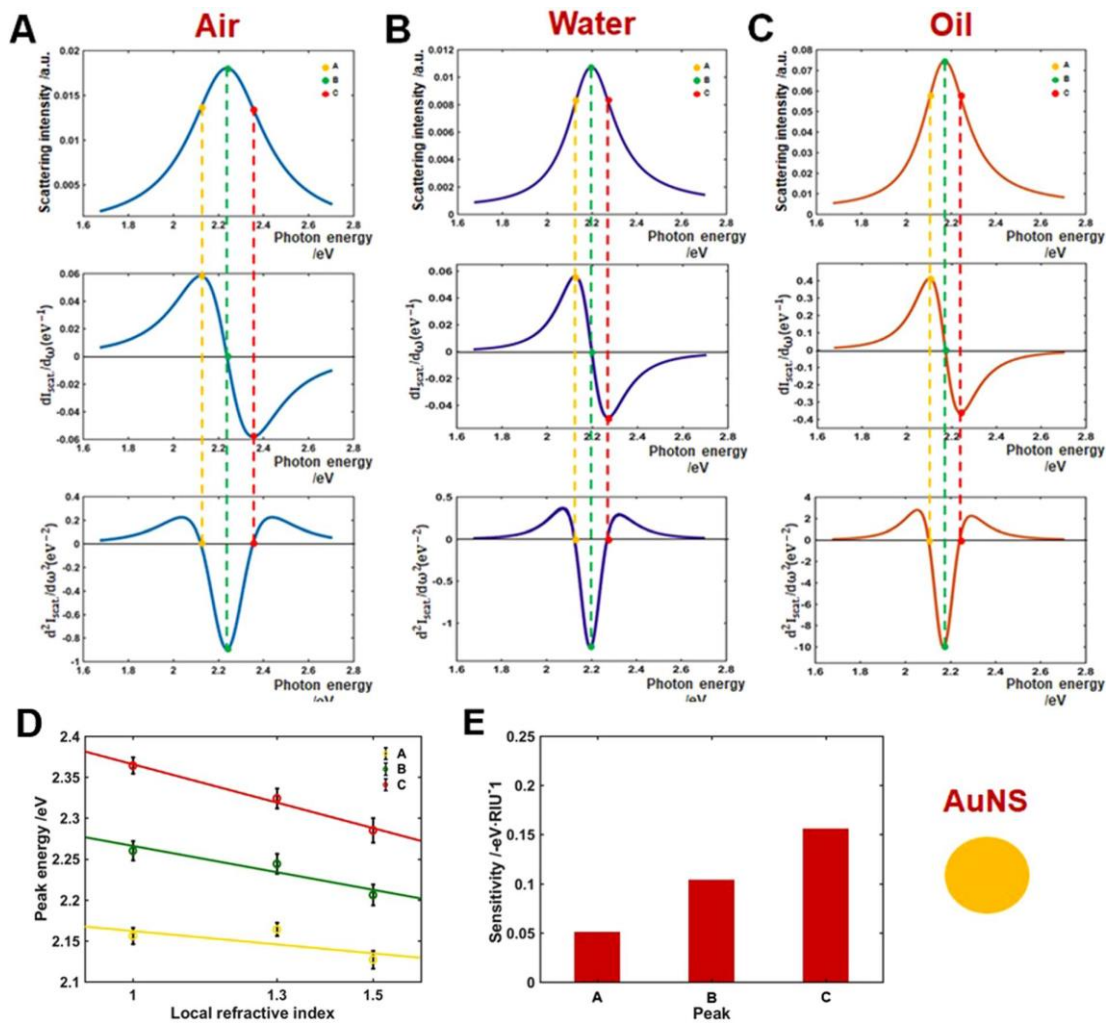


**Fig. 10** Inflection point method for single particle LSPR scattering sensing with AuNSs in the three local refractive indexes (air, water, and oil). (A–C) LSPR scattering efficiencies (first row), and its first (second row), and second (third row) order derivatives. (D) Peak energy plotted against the three local RI for points A, B, and C. (E) Sensitivity of local RI media on peak shifts A, B and C.

Next, to better understand the shape-dependent RI sensitivity at the LSPR IFs, DF microscopy and spectroscopy experiments were performed for AuNCs with vertices. The RI sensitivity of LSPR IFs of AuNSs was compared with that of AuNCs with vertices. Both AuNSs and AuNCs of similar size showed a single broad LSPR peak at similar LSPR wavelengths; therefore, this investigation focuses on how the shape of the nanoparticles (e.g., vertices, edges, etc.) affects the RI sensitivity at LSPR IFs at the single particle level. Similar to the analysis method used for AuNSs in Fig. 10, the first and second derivatives of the experimental LSPR scattering spectra of AuNCs with vertices were obtained. The first, second, and third rows in Fig. 11A–C show the scattering spectra of single AuNCs and the corresponding first and second order derivatives, respectively. The maxima of the LSPR scattering peak in the three local RI media, B, are located at 2.225, 2.190, and 2.155 eV for the three local environments (air, water, and oil). The local maxima and minima of the first order derivatives flanking the LSPR peak maxima (B), represented by A/C, are at 2.119/2.328, 2.114/2.265 and 2.085/2.225 eV for air, water, and oil, respectively. Consequently, A and C represent the two LSPR IFs of AuNCs, yielding the zero values of the second order derivatives of the LSPR scattering spectra (third row). Measurement of the LSPR (B, maximum) scattering spectra in multiples of 10 for each local RI index provided the same results, with values of 2.233 ( $\pm 0.012$ ), 2.194 ( $\pm 0.017$ ) and 2.153 ( $\pm 0.013$ ) eV for local air, water, and oil. Similarly, the LSPR IFs, A and C, were 2.136 ( $\pm 0.011$ ) and 2.328 ( $\pm 0.017$ ),

2.119 ( $\pm 0.019$ ) and 2.268 ( $\pm 0.016$ ), and 2.082 ( $\pm 0.015$ ) and 2.224 ( $\pm 0.011$ ) eV, respectively. The peak energy A, B, and C was plotted vs. local air, water, and oil RI media. As presented in Fig. 11D, the peak energies at A, B, and C showed a linear relation with the three different local RI media. The use of a fitting function allowed to determine the slopes:  $0.064 \text{ eV}\cdot\text{RIU}^{-1}$  ( $R^2 = 0.9685$ ) for peak A,  $0.138 \text{ eV}\cdot\text{RIU}^{-1}$  ( $R^2 = 0.9868$ ) for B, and  $0.206 \text{ eV}\cdot\text{RIU}^{-1}$  ( $R^2 = 0.9998$ ) for C. Similar to the experimental result of AuNSs, the inflection point C exhibited the highest sensitivity with respect to the IF A and the LSPR peaks maxima (B) as shown in Fig. 11E (Tables 2 for full details). Interestingly, the local RI sensitivity at inflection point C was improved by 5.10% with respect to the LSPR peak maximum (B). This result is consistent with that of AuNSs (Fig. 10). Therefore, the LSPR IF C at the longer wavelength side showed higher RI sensitivity than the LSPR peak maximum (B) for both AuNSs and AuNCs. Furthermore, AuNCs with edges and vertices showed higher RI sensitivity than AuNSs of similar size at the position of LSPR IF C.

Single AuNCs	1	2	3	4	5	6	7	8	9	10	Ave	Std
Slope at Inflection A ( $\text{eV}\cdot\text{RIU}^{-1}$ )	0.096	0.120	0.168	0.090	0.057	0.115	0.073	0.087	0.126	0.106	0.104	0.029
Slope at LSPR B ( $\text{eV}\cdot\text{RIU}^{-1}$ )	0.149	0.174	0.232	0.175	0.131	0.145	0.109	0.121	0.178	0.149	0.156	0.033
Slope at Inflection C ( $\text{eV}\cdot\text{RIU}^{-1}$ )	0.204	0.228	0.297	0.258	0.197	0.172	0.148	0.155	0.222	0.190	0.207	0.044

**Table 2.** Local refractive index Sensitivities of single AuNCs at each point (first inflection point A, LSPR peak B, second inflection point C)

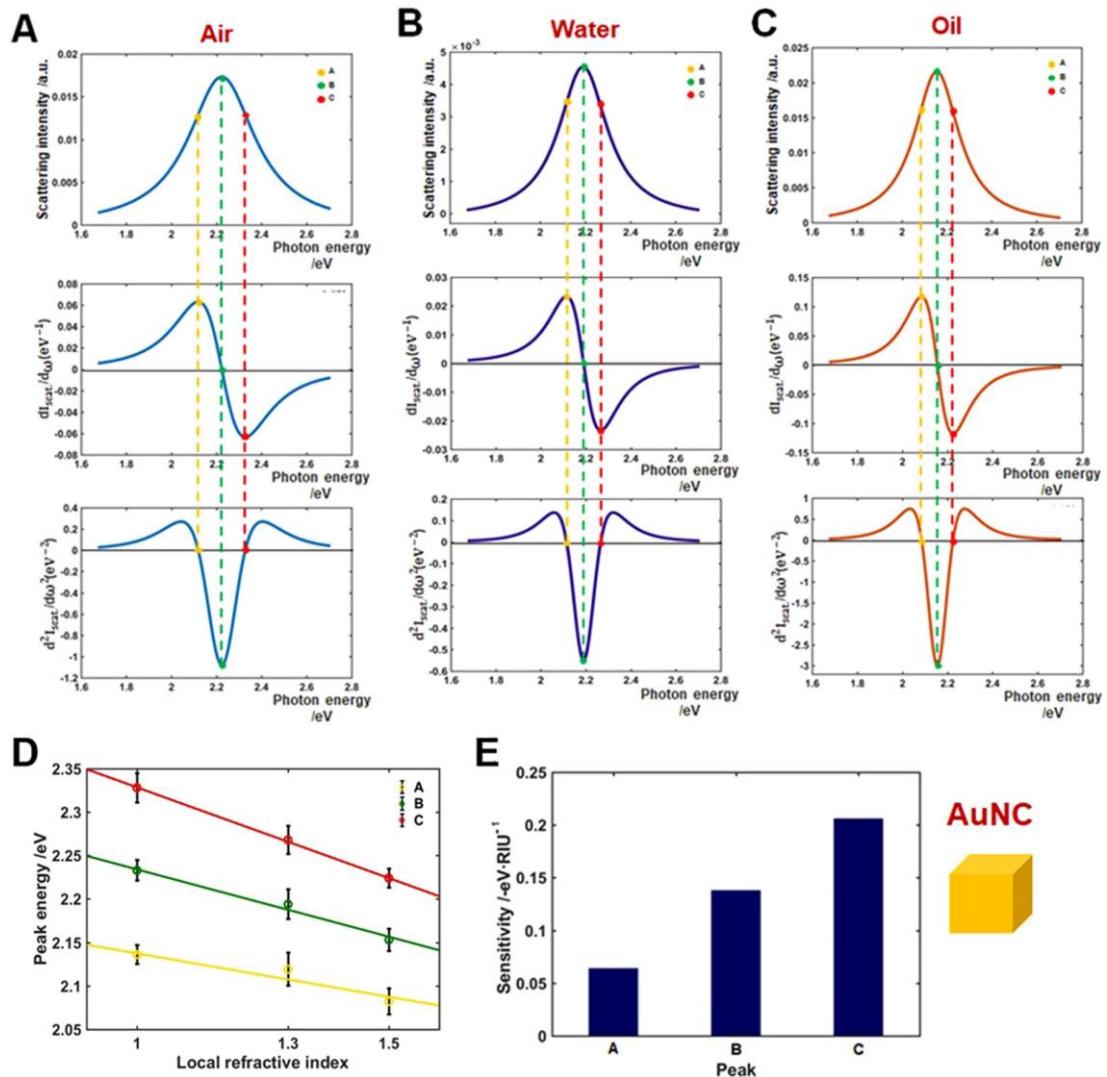


**Fig. 11** Inflection point method for single particle LSPR scattering sensing with AuNCs in the three local refractive indexes (air, water, and oil). (A–C) LSPR scattering efficiencies (first row), and its first (second row), and second (third row) order derivatives. (D) Peak energy plotted against the three local RI for points A, B, and C. (E) Sensitivity of local RI media on peak shifts A, B and C.

### 3.3. Encapsulation-Release Identification of Guest Molecules Using Chemical Interface Damping Effect between Gold Nanoparticles and Host-Guest Complex

SEM image and UV-Vis spectrum of the 25 nm × 73 nm AuNRs used in this experiment are shown in Fig. 12A and B. The anticancer drug used as a guest material in this experiment is oxaliplatin<sup>36,37</sup>, whose chemical structure and UV-Vis spectrum are shown in Fig. 12C, D. The oxaliplatin among platinum anticancer drugs (cisplatin<sup>45,46</sup>, carboplatin, nedaplatin, oxaliplatin) has the only Gibbs free energy of formation negative value (-0.590 kcal mol<sup>-1</sup>) for CB[7] in aqueous solution. (cisplatin: 80.73 kcal mol<sup>-1</sup>, carboplatin: 84.85 kcal mol<sup>-1</sup>, nedaplatin: 87.33 kcal mol<sup>-1</sup>)<sup>47</sup> In this experiment, oxaliplatin is more suitable than other Pt-drugs because we used the dipping method of the guest solution as sample preparation. The results of this experiment with cisplatin and oxaliplatin also support these results (Fig. 15 and Table 3).

Sequential experimental sample preparation is shown in Scheme 2. Fig. 1 shows structure of CB[7]-NH<sub>2</sub>. In case of single AuNRs surrounded by CTAB capping materials, DF scattering intensity was measured the highest (Fig. 13B, yellow). After CB[7]-NH<sub>2</sub> was attached, intensity reduction and red shift were observed (Fig. 13B, Blue)<sup>22</sup> and then after oxaliplatin was encapsulated, further decrease in intensity and red shift were observed (Fig. 13B, Red). As shown in Fig. 14C, the FWHM value was the narrowest at 90.060 meV for single AuNRs, and after CB[7]-NH<sub>2</sub> attached to the surface of AuNRs, a linewidth broadening was observed at 114.698 meV.<sup>24</sup> Also, after encapsulation of oxaliplatin, additional broadening of

FWHM 126.714 meV was observed. This goes beyond the work of applying CID only to materials attached directly to gold nanoparticles and provides new information on the indirect effects of guest materials by complexes on CID.

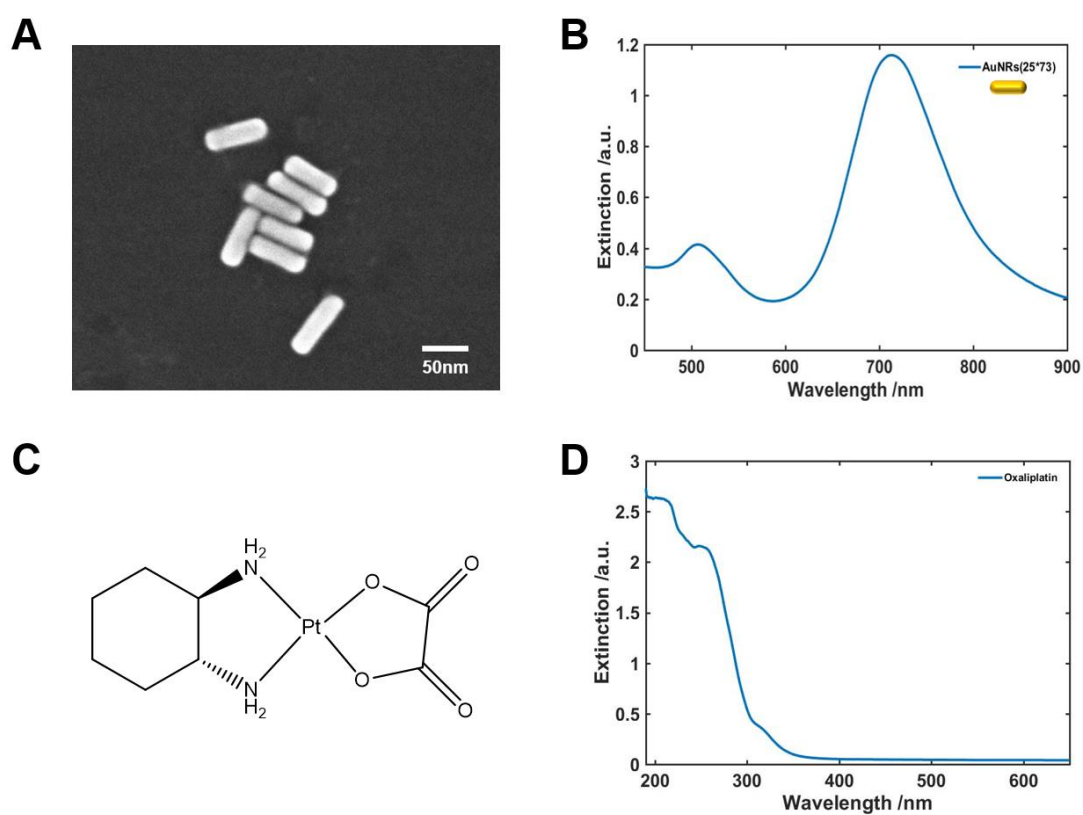
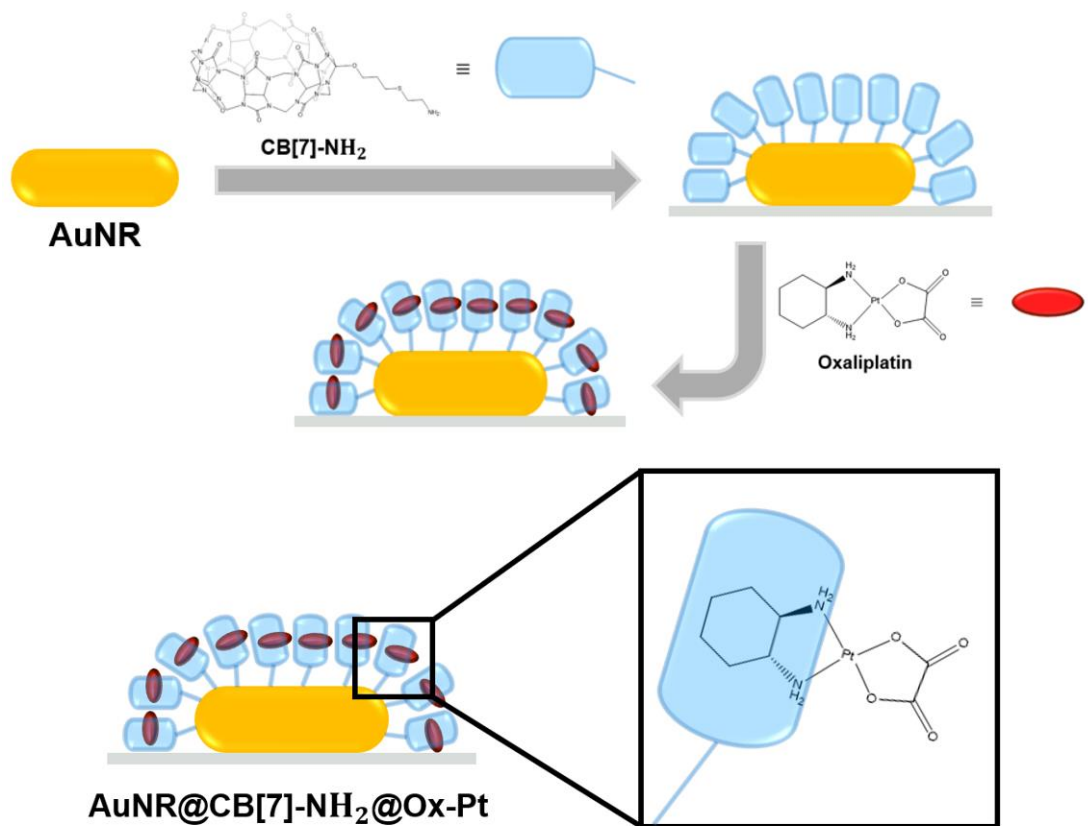


**Fig. 12** (A) SEM image of single AuNRs with aspect ratio 25nm  $\times$  73 nm. (C) Chemical structure of oxaliplatin. UV-Vis extinction spectra of the AuNRs (B) and oxaliplatin (D) dispersed in water.



**Scheme 2.** Schematic to show sequential sample preparation to encapsulate oxaliplatin into CB[7]-NH<sub>2</sub>.

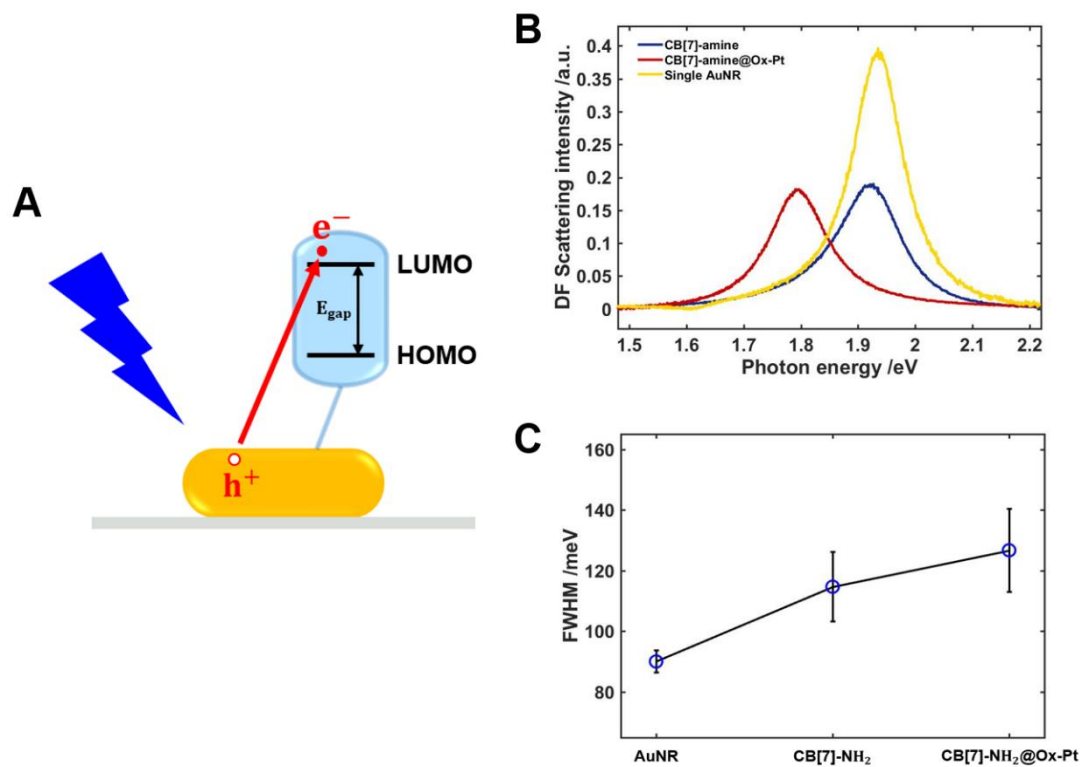
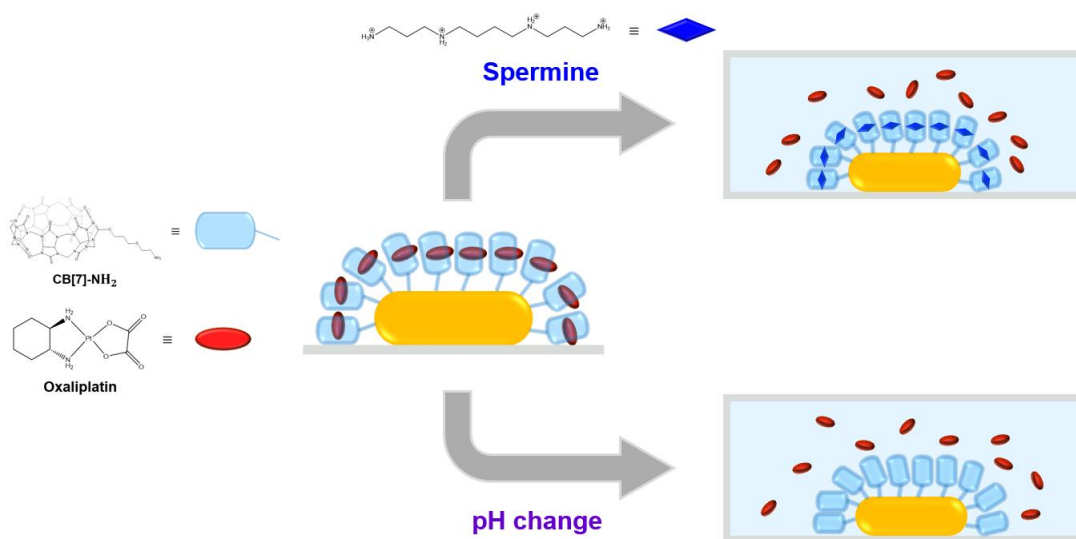


**Fig. 13** (A) Schematic to show CID phenomenon between AuNR and CB[7]-NH<sub>2</sub>. (B) Comparison of DF scattering spectra among single AuNRs capped by CTAB, attached with CB[7]-NH<sub>2</sub> and with complex (CB[7]-NH<sub>2</sub>@Ox-Pt). (C) Comparison of FWHM value about single AuNRs capped by CTAB, single AuNRs attached with CB[7]-NH<sub>2</sub> and attached with complex (CB[7]-NH<sub>2</sub>@Ox-Pt).

In order to release the drug from the complex, a total of two methods were attempted by introducing a competitive guest molecule<sup>48</sup> and changing pH<sup>49, 50</sup> (Scheme 3). The reasons of using spermine as competitive guest materials were that spermine is overexpressed tumor biomarkers for cancer cells such as colorectal tumors and lung tumors and is with good binding constant with CB [7]. Oxaliplatin and spermine had  $K_a$  values of  $2.89 \times 10^6 \text{ M}^{-1}$  and  $1.18 \times 10^6 \text{ M}^{-1}$  for CB [7] at pH 6.0 PBS buffer solution at  $37.0^\circ \text{C}$ .<sup>48</sup> In this experiment, the concentration of spermine solution was used 50 times higher than oxaliplatin to induce the release of oxaliplatin.

In Fig. 14, the encapsulation of oxaliplatin can be estimated by increasing the intensity and slight red shift when CB[7]-NH<sub>2</sub> is added to oxaliplatin (black, yellow). And when excess spermine is added to the complex solution, the peak of oxaliplatin disappears and the peak by spermine is slightly revealed (purple). Through these results we can confirm the release of oxaliplatin from the complex by the added spermine.

In the DF measurement at single particle level (Fig. 15) as well as UV-Vis experiments, the release of oxaliplatin by spermine was demonstrated by the decrease of FWHM value from 126.714 meV to 118.654 meV when spermine was added. Control experiment results in case of attaching just spermine on the surface of AuNRs, FWHM value of 111.926 meV and spermine encapsulated value of 113.488 meV in CB[7]-NH<sub>2</sub> indicate that oxaliplatin being into complex was replaced by excess spermine.



**Scheme 3.** Schematic of release of Ox-Pt from complex (CB[7]-NH<sub>2</sub>@Ox-Pt). Two methods are used to induce release of Ox-Pt. One is using spermine as competitive guest materials and the other is pH changes.

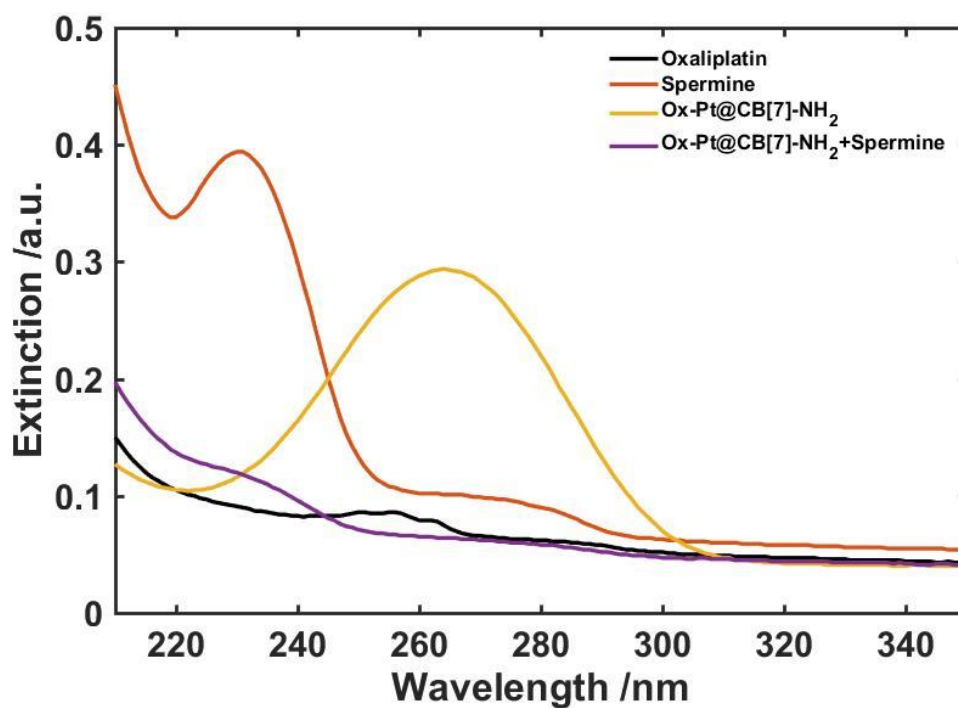


**Fig. 14** UV-Vis spectra of oxaliplatin, spermine and their respective complex. Intensity increase and Red shift indicate encapsulation of oxaliplatin into CB[7]-NH<sub>2</sub> (Black, Yellow). After adding spermine into complex of oxaliplatin, disappearance of oxaliplatin peak suggests release of oxaliplatin from complex (Purple).

Next, the pH change was used to induce the release of oxaliplatin only from the complex. (Scheme 3) As a result of changing the pH of the complex solution (pH 7) to pH 5 and pH 9, the release of oxaliplatin was confirmed. The experimental results are shown in Fig. 15 and Table 3. When the FWHM value of oxaliplatin-encapsulated complex solution with pH 7 was changed from 126.714 meV to pH 5 and pH 9, it was reduced to 117.029 meV and 118.765 meV, respectively. These values are closer to FWHM 114.698 meV with only CB[7]-NH<sub>2</sub> attached to the surface of single AuNRs. This decrease in FWHM supports the release of some oxaliplatin from the complex depending on pH changes.

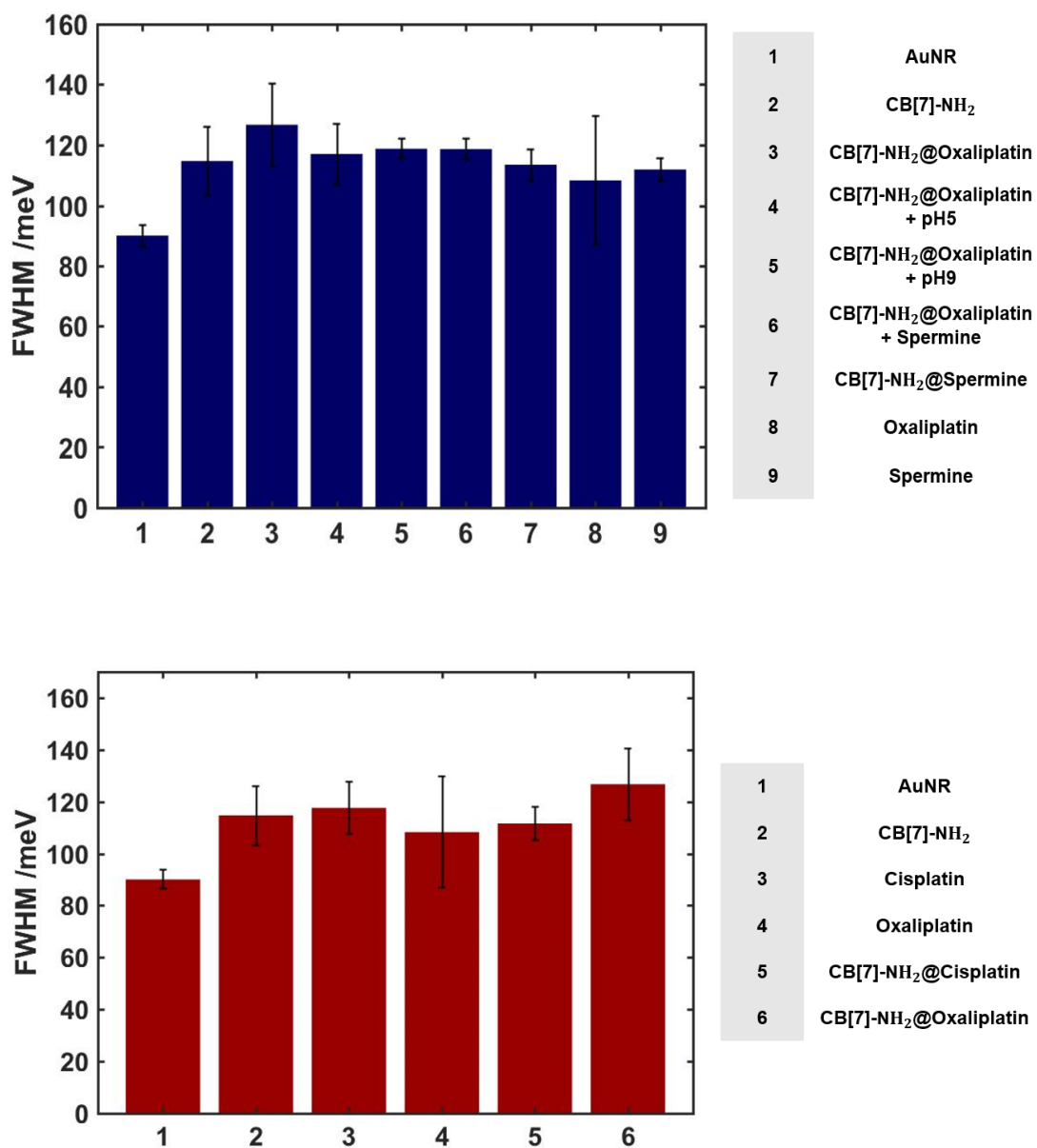


**Fig. 15** Full width at half maximum change by encapsulation and release of Ox-Pt from complex.

<b>Sample</b>	<b>Average FWHM (meV)</b>
Single AuNRs	90.060 ( $\pm 3.6$ )
CB[7]-NH <sub>2</sub>	114.698 ( $\pm 11.4$ )
CB[7]-NH <sub>2</sub> + Ox-Pt	126.714 ( $\pm 13.7$ )
Ox-Pt	108.276 ( $\pm 21.3$ )
CB[7]-NH <sub>2</sub> + Spermine	113.488 ( $\pm 5.2$ )
Spermine	111.926 ( $\pm 3.7$ )
CB[7]-NH <sub>2</sub> + Cisplatin	111.617 ( $\pm 6.3$ )
Cisplatin	117.630 ( $\pm 10.1$ )
CB[7]-NH <sub>2</sub> + Ox-Pt (pH5)	117.029 ( $\pm 10.1$ )
CB[7]-NH <sub>2</sub> + Ox-Pt (pH9)	118.765 ( $\pm 3.3$ )
CB[7]-NH <sub>2</sub> + Ox-Pt (+Spermine)	118.654 ( $\pm 3.4$ )

**Table 3.** Average FWHM value(meV) depending on each attached material on the surface of single AuNRs.

### 3.4. Correlation Between CID and Binding Constants and Charge Effect of Guest Materials

Guest molecules with four kinds of amine groups with each different binding constant and + charge number for CB[6] were used in this experiment. The chemical structure of the guest materials is shown in Fig. 18. The binding constant for CB [6] in water solution is that spermine tetrahydrochloride (G1) is  $(3.4 \pm 0.5) \times 10^{12}$ , spermidine trihydrochloride (G2) is  $(4.8 \pm 0.3) \times 10^{11}$ , 1,4-diaminobutane dihydrochloride (G3) is  $(2.3 \pm 0.3) \times 10^{10}$  and n-pentyl ammonium chloride (G4) is  $(3.0 \pm 0.1) \times 10^8$ .<sup>38</sup> According to the number of ammonium ions, the number of + charges decreases from four to one from G1 to G4. If we use CB[6]-NH<sub>2</sub> as CB[6], guest materials with amine groups can remove CB [6]-NH<sub>2</sub> from the AuNR surface. Therefore, to minimize the variables that can be caused by the guest materials with the amine group, we used CB[6]-SH with thiol groups because thiol has a higher binding strength with Au than amine. Chemical structure of CB[6]-SH is shown in Fig. 1.

After attaching CB[6]-SH on the AuNR surface, samples were prepared in the order of encapsulation of the guest materials into CB[6]-SH. When CB[6]-SH is attached to the AuNR surface, the broadening of FWHM was observed from 90.060 meV to 123.788 meV. This result suggested materials adhered well to the surface of AuNRs from linewidth broadening by CID.<sup>22, 24</sup> After encapsulation of guest materials (G1 ~ G4), the results that measured the FWHM values are each 121.459 meV, 118.093 meV, 111.348 meV, 106.121 meV.

These experimental results show that the CID phenomenon of CB[6]-SH by the guest materials is proportional to the binding constant and the number of + charges. Each experimental result is shown in Fig 17 and Table 4.

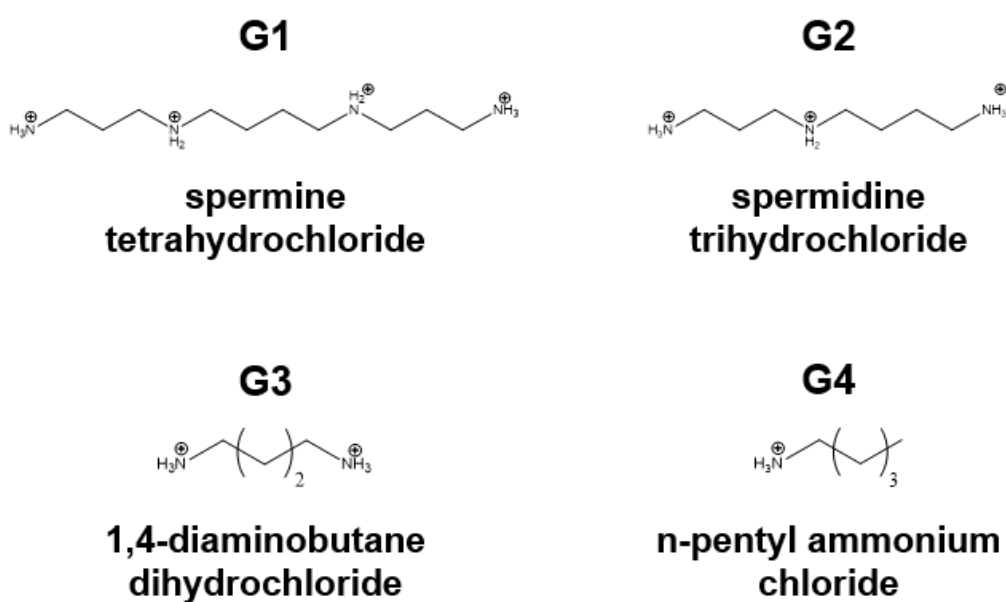


**Fig. 16** Chemical structure of guest materials with amine groups.

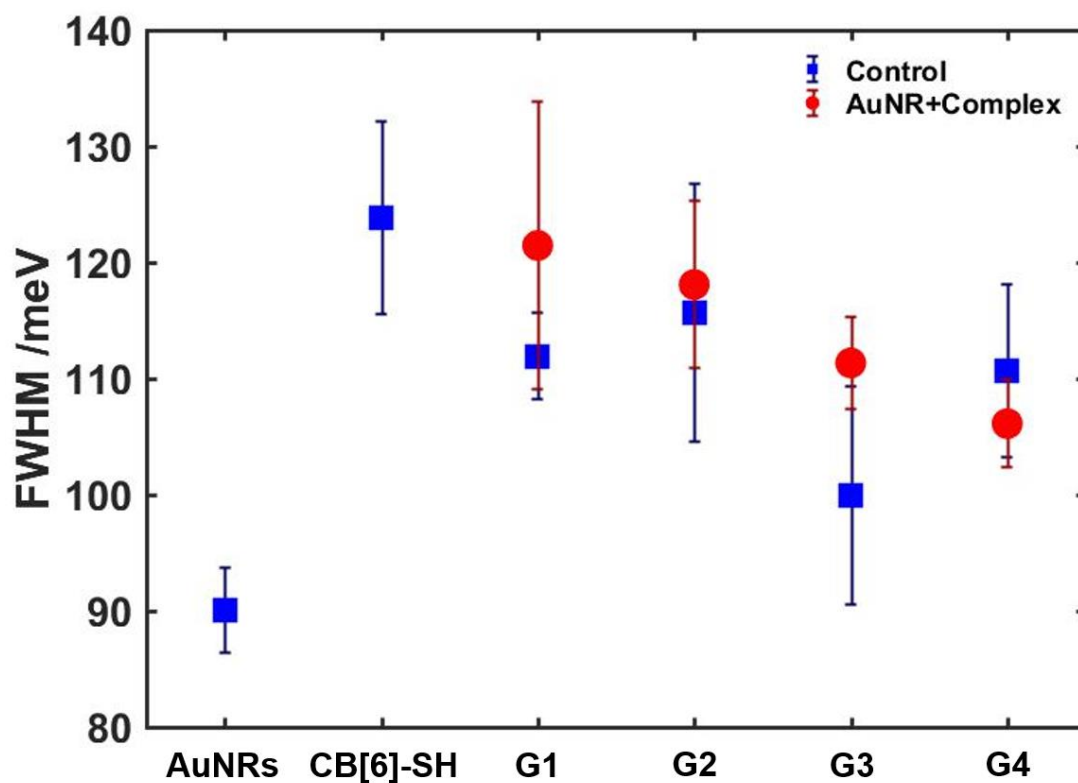


**Fig. 17** Comparison of total experimental results. Blue squares are control experiment and red circles are encapsulation of guest materials into CB[6]-SH. The more binding constant and charge number of guest materials with amine groups increase, the more FWHM is broaden. Binding constant and charge effect increase from G4 to G1. (G1: spermine tetrahydrochloride, G2: spermidine trihydrochloride, G3: 1,4-diaminobutane dihydrochloride, G4: n-pentyl ammonium chloride)

Sample	Average FWHM (meV)
Single AuNRs	90.060 ( $\pm 3.6$ )
CB[6]-SH	123.788 ( $\pm 8.3$ )
CB[6]-SH + G1	121.459 ( $\pm 12.4$ )
G1	111.926 ( $\pm 3.7$ )
CB[6]-SH + G2	118.093 ( $\pm 7.2$ )
G2	115.652 ( $\pm 11.1$ )
CB[6]-SH + G3	111.348 ( $\pm 4.0$ )
G3	99.935 ( $\pm 9.4$ )
CB[6]-SH + G4	106.121 ( $\pm 3.8$ )
G4	110.677 ( $\pm 7.4$ )

**Table 4.** Average FWHM value (meV) depending on each attached material on the surface of single AuNRs. (G1: spermine tetrahydrochloride, G2: spermidine trihydrochloride, G3: 1,4-diaminobutane dihydrochloride, G4: n-pentyl ammonium chloride)

## 4. Conclusions

In conclusion, we studied improving method of RI sensitivity and application of CID effect.

First, we characterized the optical properties of single AuNCs with an average diameter of 50 nm by single-particle DF microscopy and spectroscopy. A broad and symmetrical LSPR peak was observed at about 560 nm for single AuNCs. Furthermore, we carried out real-time studies to monitor the binding events of 1-decanethiol in ethanol on single AuNCs. The thiol molecules strongly reduced the scattering intensity because of adsorption of the adsorbate on the AuNC. Furthermore, the homogeneous LSPR linewidth of single AuNCs was broadened due to the CID effect. These results allow us to better understand the CID effect in AuNCs with edges and vertices at the single particle level.

Second, we demonstrated the significance of tracking the curvature shapes through homogeneous LSPR IFs near the resonance energy in various local RIs (air, water, oil), rather than tracking their counterpart LSPR maximum peak shifts, for both AuNSs and AuNCs of similar size. The homogeneous LSPR scattering IFs of single gold nanoparticles (AuNSs, AuNCs) with a single resonant mode showed an enhanced RI sensitivity in various local RI environments. Furthermore, we found that single AuNCs with sharp vertices and edges showed higher RI sensitivity at homogeneous LSPR IFs than single AuNSs, with no edges, of similar size. Therefore, this study provides a deep insight into shape-dependent RI sensitivity of

homogeneous LSPR IFs in single Au nanoparticles having a single resonant mode using DF single particle spectroscopy. Moreover, we showed that tracking the curvature changes in the LSPR scattering spectra of single AuNCs with vertices may be effectively employed in LSPR-based RI sensing studies.

Third, we introduced host molecules such as CB[7]-NH<sub>2</sub> as a way to improve the stability of anticancer drugs such as oxaliplatin and confirmed encapsulation by measuring CID effect using gold nanoparticles. In addition, drug release important in the drug delivery system (DDS) was induced by using spermine in large amounts in cancer cells and pH changes. When oxaliplatin was encapsulated, additional FWHM broadening was observed, and two kinds of methods showed that the linewidth was narrower than that of the complex when inducing release. Therefore, this study provides a new way to measure encapsulation and release of drugs into host substances. In addition, it provides greater understanding and insight into CID phenomena because it gives information about the indirect effects of guest materials in attached complexes, not directly attached materials as well as shows the applicability to DDS.

Finally, we performed experiments using CB[6]-SH and four types of guest materials to determine the correlation between binding constant, charge effect and CID phenomenon between host and guest materials. It was confirmed that linewidth broadening by CID phenomenon occurs as binding constants and the number of + charges increases for the total of four kinds of guest molecules having amine groups. Although it is a method that can be measured in the state of knowing a substance, the

results of such experiments are meaningful because there is still no way to distinguish amine groups. Therefore, these results suggest the possibility of differentiating molecules having amine groups and show the correlation between the binding constant, charge effect and CID phenomenon. It also provides applicability by providing additional information about the CID.

## 5. References

1. Nehl, C. L.; Liao, H.; Hafner, J. H., Optical properties of star-shaped gold nanoparticles. *Nano letters* **2006**, *6* (4), 683-688.
2. Nehl, C. L.; Hafner, J. H., Shape-dependent plasmon resonances of gold nanoparticles. *Journal of Materials Chemistry* **2008**, *18* (21), 2415-2419.
3. Sosa, I. O.; Noguez, C.; Barrera, R. G., Optical properties of metal nanoparticles with arbitrary shapes. *The Journal of Physical Chemistry B* **2003**, *107* (26), 6269-6275.
4. Noguez, C., Surface Plasmons on Metal Nanoparticles: The Influence of Shape and Physical Environment. *The Journal of Physical Chemistry C* **2007**, *111* (10), 3806-3819.
5. Zhang, X.-F.; Liu, Z.-G.; Shen, W.; Gurunathan, S., Silver nanoparticles: synthesis, characterization, properties, applications, and therapeutic approaches. *International journal of molecular sciences* **2016**, *17* (9), 1534.
6. Boyer, D.; Tamarat, P.; Maali, A.; Lounis, B.; Orrit, M., Photothermal imaging of nanometer-sized metal particles among scatterers. *Science* **2002**, *297* (5584), 1160-1163.
7. Chang, W.-S.; Ha, J. W.; Slaughter, L. S.; Link, S., Plasmonic nanorod absorbers as orientation sensors. *Proceedings of the National Academy of Sciences* **2010**, *107* (7), 2781-2786.
8. Ringe, E.; McMahon, J. M.; Sohn, K.; Cobley, C.; Xia, Y.; Huang, J.; Schatz, G. C.; Marks, L. D.; Van Duyne, R. P., Unraveling the effects of size, composition, and substrate on the localized surface plasmon resonance frequencies of gold and silver nanocubes: a systematic single-particle approach. *The Journal of Physical Chemistry C* **2010**, *114* (29), 12511-12516.
9. Kooij, E. S.; Ahmed, W.; Hellenthal, C.; Zandvliet, H. J.; Poelsema, B., From nanorods to nanostars: Tuning the optical properties of gold nanoparticles. *Colloids and surfaces A: Physicochemical and engineering aspects* **2012**, *413*, 231-238.
10. Jazayeri, M. H.; Amani, H.; Pourfatollah, A. A.; Pazoki-Toroudi, H.; Sedighimoghaddam, B., Various methods of gold nanoparticles (GNPs) conjugation to antibodies. *Sensing and bio-sensing research* **2016**, *9*, 17-22.
11. Lee, D.-E.; Koo, H.; Sun, I.-C.; Ryu, J. H.; Kim, K.; Kwon, I. C., Multifunctional nanoparticles for multimodal imaging and theragnosis. *Chemical Society Reviews* **2012**, *41* (7), 2656-2672.
12. Chen, Y.; Xianyu, Y.; Jiang, X., Surface modification of gold nanoparticles with small molecules for biochemical analysis. *Accounts of chemical research* **2017**, *50* (2),

310-319.

13. Sperling, R. A.; Parak, W. J., Surface modification, functionalization and bioconjugation of colloidal inorganic nanoparticles. *Philosophical Transactions of the Royal Society A: Mathematical, Physical and Engineering Sciences* **2010**, *368* (1915), 1333-1383.
14. Jans, H.; Huo, Q., Gold nanoparticle-enabled biological and chemical detection and analysis. *Chemical Society Reviews* **2012**, *41* (7), 2849-2866.
15. Soares, L.; Csáki, A.; Jatschka, J.; Fritzsche, W.; Flores, O.; Franco, R.; Pereira, E., Localized surface plasmon resonance (LSPR) biosensing using gold nanotriangles: detection of DNA hybridization events at room temperature. *Analyst* **2014**, *139* (19), 4964-4973.
16. Nusz, G. J.; Curry, A. C.; Marinakos, S. M.; Wax, A.; Chilkoti, A., Rational selection of gold nanorod geometry for label-free plasmonic biosensors. *ACS nano* **2009**, *3* (4), 795-806.
17. Yang, S.; Wu, T.; Zhao, X.; Li, X.; Tan, W., The optical property of core-shell nanosensors and detection of atrazine based on localized surface plasmon resonance (LSPR) sensing. *Sensors* **2014**, *14* (7), 13273-13284.
18. Hu, M.; Novo, C.; Funston, A.; Wang, H.; Staleva, H.; Zou, S.; Mulvaney, P.; Xia, Y.; Hartland, G. V., Dark-field microscopy studies of single metal nanoparticles: understanding the factors that influence the linewidth of the localized surface plasmon resonance. *Journal of materials chemistry* **2008**, *18* (17), 1949-1960.
19. Zhang, L.; Wang, J.; Zhang, J.; Liu, Y.; Wu, L.; Shen, J.; Zhang, Y.; Hu, Y.; Fan, Q.; Huang, W.; Wang, L., Individual Au-Nanocube Based Plasmonic Nanoprobe for Cancer Relevant MicroRNA Biomarker Detection. *ACS Sensors* **2017**, *2* (10), 1435-1440.
20. Cennamo, N.; Agostino, G.; Donà, A.; Dacarro, G.; Pallavicini, P.; Pesavento, M.; Zeni, L., Localized Surface Plasmon Resonance with Five-Branched Gold Nanostars in a Plastic Optical Fiber for Bio-Chemical Sensor Implementation. *Sensors* **2013**, *13* (11).
21. Dondapati, S. K.; Sau, T. K.; Hrelescu, C.; Klar, T. A.; Stefani, F. D.; Feldmann, J., Label-free Biosensing Based on Single Gold Nanostars as Plasmonic Transducers. *ACS Nano* **2010**, *4* (11), 6318-6322.
22. Foerster, B.; Joplin, A.; Kaefer, K.; Celiksoy, S.; Link, S.; Sönnichsen, C., Chemical Interface Damping Depends on Electrons Reaching the Surface. *ACS Nano* **2017**, *11* (3), 2886-2893.
23. Zhang, Y.; He, S.; Guo, W.; Hu, Y.; Huang, J.; Mulcahy, J. R.; Wei, W. D., Surface-Plasmon-Driven Hot Electron Photochemistry. *Chemical Reviews* **2018**, *118* (6),

2927-2954.

24. Boerigter, C.; Aslam, U.; Linic, S., Mechanism of Charge Transfer from Plasmonic Nanostructures to Chemically Attached Materials. *ACS Nano* **2016**, *10* (6), 6108-6115.
25. Slaughter, L.; Chang, W.-S.; Link, S., Characterizing Plasmons in Nanoparticles and Their Assemblies with Single Particle Spectroscopy. *The Journal of Physical Chemistry Letters* **2011**, *2* (16), 2015-2023.
26. Chen, P.; Liedberg, B., Curvature of the localized surface plasmon resonance peak. *Analytical chemistry* **2014**, *86* (15), 7399-7405.
27. Derkachova, A.; Kolwas, K.; Demchenko, I., Dielectric function for gold in plasmonics applications: size dependence of plasmon resonance frequencies and damping rates for nanospheres. *Plasmonics* **2016**, *11* (3), 941-951.
28. Alabastri, A.; Tuccio, S.; Giugni, A.; Toma, A.; Liberale, C.; Das, G.; Angelis, F. D.; Fabrizio, E. D.; Zaccaria, R. P., Molding of plasmonic resonances in metallic nanostructures: Dependence of the non-linear electric permittivity on system size and temperature. *Materials* **2013**, *6* (11), 4879-4910.
29. Chen, P.; Tran, N. T.; Wen, X.; Xiong, Q.; Liedberg, B., Inflection point of the localized surface plasmon resonance peak: a general method to improve the sensitivity. *ACS sensors* **2017**, *2* (2), 235-242.
30. Juvé, V.; Cardinal, M. F.; Lombardi, A.; Crut, A.; Maioli, P.; Pérez-Juste, J.; Liz-Marzán, L. M.; Del Fatti, N.; Vallée, F., Size-dependent surface plasmon resonance broadening in nonspherical nanoparticles: single gold nanorods. *Nano letters* **2013**, *13* (5), 2234-2240.
31. Tsalu, P. V.; Kim, G. W.; Hong, J. W.; Ha, J. W., Homogeneous localized surface plasmon resonance inflection points for enhanced sensitivity and tracking plasmon damping in single gold bipyramids. *Nanoscale* **2018**, *10* (26), 12554-12563.
32. Yu, G.; Jie, K.; Huang, F., Supramolecular amphiphiles based on host-guest molecular recognition motifs. *Chemical reviews* **2015**, *115* (15), 7240-7303.
33. Ma, X.; Zhao, Y., Biomedical applications of supramolecular systems based on host-guest interactions. *Chemical reviews* **2014**, *115* (15), 7794-7839.
34. Jeon, Y.-M.; Kim, J.; Whang, D.; Kim, K., Molecular container assembly capable of controlling binding and release of its guest molecules: reversible encapsulation of organic molecules in sodium ion complexed cucurbituril. *Journal of the American Chemical Society* **1996**, *118* (40), 9790-9791.
35. Konda, S. K.; Maliki, R.; McGrath, S.; Parker, B. S.; Robinson, T.; Spurling, A.; Cheong, A.; Lock, P.; Pigram, P. J.; Phillips, D. R., Encapsulation of mitoxantrone within

- cucurbit [8] uril decreases toxicity and enhances survival in a mouse model of cancer. *ACS medicinal chemistry letters* **2017**, *8* (5), 538-542.
36. Jeon, Y. J.; Kim, S.-Y.; Ko, Y. H.; Sakamoto, S.; Yamaguchi, K.; Kim, K., Novel molecular drug carrier: encapsulation of oxaliplatin in cucurbit [7] uril and its effects on stability and reactivity of the drug. *Organic & biomolecular chemistry* **2005**, *3* (11), 2122-2125.
37. Brown, S. D.; Nativio, P.; Smith, J.-A.; Stirling, D.; Edwards, P. R.; Venugopal, B.; Flint, D. J.; Plumb, J. A.; Graham, D.; Wheate, N. J., Gold nanoparticles for the improved anticancer drug delivery of the active component of oxaliplatin. *Journal of the American Chemical Society* **2010**, *132* (13), 4678-4684.
38. Kim, Y.; Kim, H.; Ko, Y. H.; Selvapalam, N.; Rekharsky, M. V.; Inoue, Y.; Kim, K., Complexation of aliphatic ammonium ions with a water-soluble cucurbit [6] uril derivative in pure water: isothermal calorimetric, NMR, and X-ray crystallographic study. *Chemistry—A European Journal* **2009**, *15* (25), 6143-6151.
39. Porter, M. D.; Bright, T. B.; Allara, D. L.; Chidsey, C. E., Spontaneously organized molecular assemblies. 4. Structural characterization of n-alkyl thiol monolayers on gold by optical ellipsometry, infrared spectroscopy, and electrochemistry. *Journal of the American Chemical Society* **1987**, *109* (12), 3559-3568.
40. Kondo, T.; Yanagida, M.; Shimazu, K.; Uosaki, K., Determination of thickness of a self-assembled monolayer of dodecanethiol on Au (111) by angle-resolved X-ray photoelectron spectroscopy. *Langmuir* **1998**, *14* (19), 5656-5658.
41. Arce, F. T.; Vela, M.; Salvarezza, R.; Arvia, A., Dynamic characteristics of adsorbed monolayers of 1-dodecanethiol on gold (111) terraces from in-situ scanning tunneling microscopy imaging. *Electrochimica acta* **1998**, *44* (6-7), 1053-1067.
42. Schwartz, D. K., Mechanisms and kinetics of self-assembled monolayer formation. *Annual Review of Physical Chemistry* **2001**, *52* (1), 107-137.
43. Jeon, H. B.; Ha, J. W., Single-Particle Study: Plasmon Damping of Gold Nanocubes with Vertices by Adsorbate Molecules. *Bulletin of the Korean Chemical Society* **2018**, *39* (9), 1117-1119.
44. McFarland, A. D.; Van Duyne, R. P., Single silver nanoparticles as real-time optical sensors with zeptomole sensitivity. *Nano letters* **2003**, *3* (8), 1057-1062.
45. Wheate, N. J.; Buck, D. P.; Day, A. I.; Collins, J. G., Cucurbit [n] uril binding of platinum anticancer complexes. *Dalton transactions* **2006**, (3), 451-458.
46. Plumb, J. A.; Venugopal, B.; Oun, R.; Gomez-Roman, N.; Kawazoe, Y.; Venkataramanan, N. S.; Wheate, N. J., Cucurbit [7] uril encapsulated cisplatin overcomes

- cisplatin resistance via a pharmacokinetic effect. *Metallomics* **2012**, *4* (6), 561-567.
47. Venkataramanan, N. S.; Ambigapathy, S.; Mizuseki, H.; Kawazoe, Y., Theoretical prediction of the complexation behaviors of antitumor platinum drugs with cucurbiturils. *The Journal of Physical Chemistry B* **2012**, *116* (48), 14029-14039.
48. Chen, Y.; Huang, Z.; Zhao, H.; Xu, J.-F.; Sun, Z.; Zhang, X., Supramolecular chemotherapy: cooperative enhancement of antitumor activity by combining controlled release of oxaliplatin and consuming of spermine by cucurbit [7] uril. *ACS applied materials & interfaces* **2017**, *9* (10), 8602-8608.
49. Liu, L., Controlled release from cucurbituril. *Journal of Inclusion Phenomena and Macrocyclic Chemistry* **2017**, *87* (1-2), 1-12.
50. Carvalho, C. P.; Uzunova, V. D.; Da Silva, J. P.; Nau, W. M.; Pischel, U., A photoinduced pH jump applied to drug release from cucurbit [7] uril. *Chemical Communications* **2011**, *47* (31), 8793-8795.